

Path-OED for infinite-dimensional Bayesian linear inverse problems governed by PDEs

J. Nicholas Neuberger^{1*}, Alen Alexanderian¹, Bart van Bloemen Waanders²,
Ahmed Attia³

¹Department of Mathematics, North Carolina State University, Raleigh, NC, USA.

²Center for Computing Research, Sandia National Laboratories, Albuquerque, NM, USA.

³Mathematics and Computer Science, Argonne National Laboratory, Lemont, IL, USA.

*Corresponding author(s). E-mail(s): jnneuber@ncsu.edu;

Abstract

We consider infinite-dimensional Bayesian linear inverse problems governed by time-dependent partial differential equations (PDEs) and develop a mathematical and computational framework for optimal design of mobile sensor paths in this setting. The proposed path optimal experimental design (path-OED) framework is established rigorously in a function space setting and elaborated for the case of Bayesian c-optimality, which quantifies the posterior variance in a linear functional of the inverse parameter. The latter is motivated by goal-oriented formulations, where we seek to minimize the uncertainty in a scalar prediction of interest. To facilitate computations, we complement the proposed infinite-dimensional framework with discretized formulations, in suitably weighted finite-dimensional inner product spaces, and derive efficient methods for finding optimal sensor paths. The resulting computational framework is flexible, scalable, and can be adapted to a broad range of linear inverse problems and design criteria. We also present extensive computational experiments, for a model inverse problem constrained by an advection-diffusion equation, to demonstrate the effectiveness of the proposed approach.

1 Introduction

Physical models governed by partial differential equations (PDEs) often contain unknown parameters that must be inferred. This requires solving an inverse problem. We consider linear Bayesian inverse problems governed by PDEs with infinite-dimensional parameters. By utilizing measurement data and a prior distribution, we apply Bayes' theorem to obtain a posterior distribution for the unknown parameter. The informativeness of the data greatly influences the quality of the solution to the inverse problem. Consequently, optimizing the data acquisition process is essential and can be framed as an optimal experimental design (OED) problem. We consider inverse problems in which data are collected using mobile sensors such as drones, human-operated devices, or robots with programmable motion.

In the present work, solving an OED problem is equivalent to minimizing an optimality criterion Ψ —a functional that quantifies uncertainty in the unknown parameter or a function of the parameter. The criterion is a function of an experimental *design vector* ξ . This vector parameterizes how data are acquired and, in our case, determines the path of a sensor. Given an admissible design set Ξ , the OED problem is

$$\operatorname{argmin}_{\xi \in \Xi} \Psi(\xi). \tag{1}$$

We consider OED problems where data acquisition is constrained to a set of permissible sensor paths. Henceforth, we use the term *path-OED* to refer to such problems.

Related work. There is a rich body of literature devoted to various aspects of OED. Textbook references on this topic include [4, 33, 44]. These books consider OED within a frequentist setting. For an overview of Bayesian OED, we refer to [12, 22]. For background and references on optimal design of infinite-dimensional Bayesian inverse problems governed by PDEs, see, e.g., [1]. The majority of recent efforts on OED for PDE-based Bayesian inverse problems concern optimal placement of static sensors.

The field of path-planning for mobile sensing platforms has become quite extensive in light of modern computational and robotic advancements. The books [13, 27, 26, 37] provide a comprehensive coverage of path-planning developments. See also [18, 23]. Methods for planning paths range from graph-based algorithms [19], trajectory parameterization [24, 40], machine and reinforcement learning [38, 43], and rapidly-exploring random trees [28]. Often, these approaches are applied to manufacturing and autonomous vehicles. There have also been works on path planning for environmental monitoring and control; see, e.g., [15].

Considerably less work has been developed in the area of path-planning of mobile sensors for the purpose of parameter identification and prediction in physical systems governed by PDEs. An early attempt at this problem is provided in [34], where optimal sensor trajectories are obtained by minimizing the log determinant of the Fischer information matrix. Subsequent works built on this idea. In particular, the books [41, 44] develop frameworks for obtaining optimal sensor trajectories in parameter estimation problems. In both works, sensor trajectories are characterized by ordinary differential equations and the optimal paths reduce a frequentist description of uncertainty in a small number of scalar-valued parameters. The paper [42] provides a concise overview of this approach. Other methods use ensembles of machine learning models or Kalman filters. In particular, optimal sensor trajectories are obtained in the work [31] using a greedy algorithm to enhance Kalman filter performance.

Our approach and contributions. We model sensor trajectories with parametric equations of the form $\mathbf{r}(t; \xi)$. Here, $t \in \mathbb{R}$ is the time variable and the parameter $\xi \in \mathbb{R}^N$ is the design parameter. The proposed path-OED framework is agnostic to the specific parameterization of \mathbf{r} and enables us to encode various constraints related to the sensor apparatus. We first formulate the path-OED problem in function space and specialize it using the c-optimality criterion, chosen for its prevalence and flexibility. While we present results for c-optimality, the framework extends to other infinite-dimensional criteria, including A- and D-optimality. The function-space setting provides a rigorous probabilistic foundation. This also guides proper choices of the prior measure and a consistent discretization strategy. In particular, upon successive mesh refinements, the discretized design criteria approximate well-defined design criteria in the function space setting. A key difference between the present path-OED problem formulation with existing works on optimal design of PDE-based inverse problems is the complex nature of the observation operator. Namely, in the present setting, the observation operator is time-dependent and is a nonlinear function of the design vector ξ . We translate the function space formulation to a discrete setting by considering suitable finite-dimensional Hilbert spaces. Subsequently, we derive novel and efficient path-tailored techniques that utilize low-rank approximations, fast solvers, and adjoint-based methods for derivative computations. The resulting computational framework is flexible, scalable, and can be adapted to a broad range of linear inverse problems.

We elaborate the proposed approach in the case of the Bayesian c-optimality criterion, which quantifies the posterior variance in a linear functional of the inversion parameter. Moreover, we investigate path constraints for two specific path parameterizations; one based on Bézier curves and the other motivated by Fourier expansions. Lastly, in our numerical results, we compute optimal sensor paths for a model inverse problem governed by a time-dependent advection diffusion equation.

The key contributions of this work are

- a rigorous and extensible mathematical framework for path-OED in infinite-dimensional linear Bayesian inverse problems (see Section 3);
- specialized techniques for two classes of parameterized paths—Bézier and Fourier—and for incorporating path constraints (see Section 4);
- a scalable computational framework for path-OED (see Section 5); and
- comprehensive computational results demonstrating the effectiveness of our approach (see Section 6).

Before detailing our proposed approach, we briefly discuss some preliminaries regarding the class of infinite-dimensional Bayesian inverse problems under study in Section 2.

2 The inverse problem

In this section we consider the problem of estimating an unknown parameter in a model governed by a linear time-dependent PDE. Herein, the governing dynamics are referred to as the *inversion model* and the unknown parameter is called the *inversion parameter*. We seek to infer the inversion parameter from discrete measurements of the inversion model state variable

We begin by introducing some notation involving linear operators on Hilbert spaces. Subsequently, we formulate the *data model* that simulates sensor measurements. This is followed by a brief description of the Bayesian approach to solving infinite-dimensional linear Bayesian inverse problems.

Notation. Let \mathcal{X} and \mathcal{Y} be infinite-dimensional real separable Hilbert spaces. We use $\mathcal{L}(\mathcal{X}, \mathcal{Y})$ to denote the Banach space of bounded linear operators from \mathcal{X} to \mathcal{Y} and $\mathcal{L}(\mathcal{X})$ as the space of bounded linear operators from \mathcal{X} to \mathcal{X} . We let $\mathcal{L}_{\text{sym}}(\mathcal{X})$ denote the space of self-adjoint bounded linear operators on \mathcal{X} , $\mathcal{L}_{\text{sym}}^+(\mathcal{X})$ the set of positive self-adjoint bounded linear operators on \mathcal{X} , $\mathcal{L}_{\text{sym}}^{++}(\mathcal{X})$ the set of *strictly* positive self-adjoint bounded linear operators on \mathcal{X} , and $\mathcal{L}_{\text{tr}}(\mathcal{X})$ as the set of trace-class operators on \mathcal{X} . Lastly, we denote the operator norm of $\mathcal{A} \in \mathcal{L}(\mathcal{X}, \mathcal{Y})$ by $\|\mathcal{A}\|$. For details on concepts from operator theory, see [36, Chapters VI–VIII].

The data model. The inversion model has a state variable $u \in \mathcal{U}$ and an inversion parameter $m \in \mathcal{M}$, where \mathcal{M} and \mathcal{U} are infinite-dimensional real separable Hilbert spaces. The *solution operator* is defined to be an element of $\mathcal{L}(\mathcal{M}, \mathcal{U})$ that maps the inversion parameter to the state that the sensor observes.

We assume that the *experimental design* (the measurement configuration) is parameterized by a design vector $\xi \in \mathbb{R}^N$. In traditional sensor placement problems, this specifies the locations of a static sensor array; in our setting, ξ instead determines the path followed by a mobile sensor (see Subsection 3.1). For $\xi \in \mathbb{R}^N$, the design induces an *observation operator*

$$\mathcal{B}(\xi) \in \mathcal{L}(\mathcal{U}, \mathbb{R}^{n_y}). \quad (2)$$

Applying $\mathcal{B}(\xi)$ to u extracts n_y discrete measurements of u at locations specified by the design. We compose the solution and observation operators to obtain the *forward operator*

$$\mathcal{F}(\xi) := \mathcal{B}(\xi) \circ \mathcal{S}, \quad \xi \in \mathbb{R}^N. \quad (3)$$

Note that $\mathcal{F} \in \mathcal{L}(\mathcal{M}, \mathbb{R}^{n_y})$ is of finite rank. Assuming an additive Gaussian error model and uncorrelated measurements, the data model is

$$\mathbf{y} = \mathcal{F}(\xi)m + \boldsymbol{\eta}, \quad \boldsymbol{\eta} \sim \mathcal{N}(\mathbf{0}, \sigma^2 \mathbf{I}). \quad (4)$$

We next specify the spaces \mathcal{M} and \mathcal{U} used in our formulations. We denote the spatial domain of the inversion model by Ω , which we assume to be an open, bounded, and convex subset of \mathbb{R}^2 . Furthermore, the temporal domain is a bounded time interval denoted by T . Subsequently, we assume that $m : \Omega \rightarrow \mathbb{R}$ and $u : \Omega \times T \rightarrow \mathbb{R}$. However, our formulations can be adapted to different setups: for example, we may consider a three-dimensional spatial domain or a time-dependent inversion parameter.

In the present work, we let $\mathcal{M} = L^2(\Omega)$ and $\mathcal{U} = L^2(\Omega \times T)$. Generally, the solutions to the inversion model lie in a Sobolev space that is a subspace of \mathcal{U} . Here, \mathcal{M} is equipped with the inner product

$$\langle f, g \rangle := \int_{\Omega} f(\mathbf{x})g(\mathbf{x}) d\mathbf{x}, \quad f, g \in \mathcal{M}, \quad (5)$$

and induced norm $\|\cdot\|_{\mathcal{M}} := \langle \cdot, \cdot \rangle^{1/2}$. Similarly, the inner product on \mathcal{U} is

$$\langle\langle u, v \rangle\rangle := \int_T \int_{\Omega} u(\mathbf{x}, t)v(\mathbf{x}, t) d\mathbf{x} dt, \quad u, v \in \mathcal{U}, \quad (6)$$

with induced norm $\|\cdot\|_{\mathcal{U}} := \langle\langle \cdot, \cdot \rangle\rangle^{1/2}$. In what follows, we will also require the Euclidean inner product of vectors \mathbf{x} and \mathbf{y} . We denote this by $\langle \mathbf{x}, \mathbf{y} \rangle_2 := \mathbf{y}^\top \mathbf{x}$.

Bayesian inversion. In the Bayesian paradigm we treat the inversion parameter as an \mathcal{M} -valued random variable and seek a posterior measure $\mu_{\text{post}}^{\mathbf{y}}$ describing the conditional distribution law of m given data \mathbf{y} . We assume a Gaussian prior measure $\mu_{\text{pr}} := \mathcal{N}(m_{\text{pr}}, \mathcal{C}_{\text{pr}})$ for m . Following the approach in [9], we define the prior covariance operator \mathcal{C}_{pr} using an elliptic differential operator of the form

$$\mathcal{E} := -a_1 \Delta + a_2 \mathcal{I}, \quad (7)$$

where $a_1, a_2 > 0$. Namely, we choose $\mathcal{C}_{\text{pr}} := \mathcal{E}^{-2}$ ensuring that $\mathcal{C}_{\text{pr}} \in \mathcal{L}_{\text{sym}}^{++}(\mathcal{M}) \cap \mathcal{L}_{\text{tr}}(\mathcal{M})$ in two- and three-dimensional computational domains.

By Bayes' theorem, the posterior measure $\mu_{\text{post}}^{\mathbf{y}, \boldsymbol{\xi}}$ is absolutely continuous with respect to μ_{pr} and its Radon–Nikodym derivative with respect to μ_{pr} satisfies

$$\frac{d\mu_{\text{post}}^{\mathbf{y}, \boldsymbol{\xi}}}{d\mu_{\text{pr}}} \propto \exp \left\{ -\frac{1}{2\sigma^2} \|\mathcal{F}(\boldsymbol{\xi})m - \mathbf{y}\|_2^2 \right\}. \quad (8)$$

See [39] for further details. Here, we have made the dependence of the posterior measure on $\boldsymbol{\xi}$ explicit.

Under the assumption of a linear model, Gaussian noise, and Gaussian prior, the posterior measure is Gaussian, with $\mu_{\text{post}}^{\mathbf{y}, \boldsymbol{\xi}} := \mathcal{N}(m_{\text{MAP}}^{\mathbf{y}}(\boldsymbol{\xi}), \mathcal{C}_{\text{post}}(\boldsymbol{\xi}))$, where both the mean and covariance admit analytic expressions [39]. Specifically,

$$\mathcal{C}_{\text{post}}(\boldsymbol{\xi}) := (\sigma^{-2}(\mathcal{F}^* \mathcal{F})(\boldsymbol{\xi}) + \mathcal{C}_{\text{pr}}^{-1})^{-1} \quad \text{and} \quad m_{\text{MAP}}^{\mathbf{y}}(\boldsymbol{\xi}) := \mathcal{C}_{\text{post}}(\sigma^{-2} \mathcal{F}^*(\boldsymbol{\xi}) \mathbf{y} + \mathcal{C}_{\text{pr}}^{-1} m_{\text{pr}}). \quad (9)$$

Here, we have also used the shorthand $(\mathcal{F}^* \mathcal{F})(\boldsymbol{\xi})$ for $[\mathcal{F}(\boldsymbol{\xi})]^* \mathcal{F}(\boldsymbol{\xi})$. Note also that $\mathcal{C}_{\text{post}} \in \mathcal{L}_{\text{sym}}^{++}(\mathcal{M}) \cap \mathcal{L}_{\text{tr}}(\mathcal{M})$.

In the Gaussian linear setting, the posterior mean coincides with the maximum a posteriori probability (MAP) point [14]. This is the motivation behind the notation for the posterior mean. The MAP point admits a variational characterization. For a $\boldsymbol{\xi} \in \mathbb{R}^N$, it can be shown that $m_{\text{MAP}}^{\mathbf{y}}(\boldsymbol{\xi})$ is the unique global minimizer of

$$J(m; \boldsymbol{\xi}) := \frac{1}{2\sigma^2} \|\mathcal{F}(\boldsymbol{\xi})m - \mathbf{y}\|_2^2 + \frac{1}{2} \langle \mathcal{C}_{\text{pr}}^{-1/2}(m - m_{\text{pr}}), \mathcal{C}_{\text{pr}}^{-1/2}(m - m_{\text{pr}}) \rangle. \quad (10)$$

Note that the domain of J is the Cameron–Martin space $\mathcal{M}_{\text{pr}} := \text{Range}(\mathcal{C}_{\text{pr}}^{1/2})$. The Hessian of J , denoted by \mathcal{H} , is an unbounded, self-adjoint, strictly positive, and densely defined operator. Two identities involving \mathcal{H} that we require are

$$\mathcal{C}_{\text{post}}(\boldsymbol{\xi}) = \mathcal{H}^{-1}(\boldsymbol{\xi}) \quad \text{and} \quad \mathcal{H}(\boldsymbol{\xi}) = \mathcal{H}_{\text{mis}}(\boldsymbol{\xi}) + \mathcal{C}_{\text{pr}}^{-1}, \quad (11)$$

where $\mathcal{H}_{\text{mis}}(\boldsymbol{\xi}) = \sigma^{-2}(\mathcal{F}^* \mathcal{F})(\boldsymbol{\xi})$ is the Hessian of the data misfit-term in (10). We remark that, for each $\boldsymbol{\xi}$, $\mathcal{H}_{\text{mis}}(\boldsymbol{\xi}) \in \mathcal{L}_{\text{sym}}^+(\mathcal{M})$ and is of finite rank. Additionally, $\mathcal{C}_{\text{pr}}^{-1}$ is a densely defined, unbounded, self-adjoint, and strictly positive operator.

The posterior covariance operator $\mathcal{C}_{\text{post}}$ and its inverse \mathcal{H} are central to the OED formulation that follows. Specifically, $\mathcal{C}_{\text{post}}$ encodes posterior uncertainty in the inversion parameter and depends on the design vector $\boldsymbol{\xi}$ through the data-misfit Hessian. Optimality criteria are expressed in terms of $\mathcal{C}_{\text{post}}$, while gradient derivations and computational methods require manipulation of \mathcal{H} .

3 The path-OED problem

As discussed in Section 1, the OED problem is given by (1). Herein, we specialize this abstract formulation by taking the design to be the trajectory of a single mobile sensor, parameterized by the *design vector* $\boldsymbol{\xi} \in \mathbb{R}^N$. The set Ξ characterizes the admissible sensor paths and solving (1) yields an optimal path.

In Subsection 3.1 we derive the observation operator in (2) that collects data along a prescribed path. To elaborate our framework, we take Ψ to be a *c*-optimality criterion [12], expressed in terms of the posterior variance of a linear functional of the inversion parameter; see Subsection 3.2. We also derive the gradient of Ψ with respect to the design vector $\boldsymbol{\xi}$ in Subsection 3.3, enabling gradient-based optimization. To facilitate this, there, we prove a more general result regarding the derivative of a parameterized covariance-like operator. Lastly, Section 3.4 specifies the particular *c*-optimality criterion used in our numerical demonstrations.

3.1 Data acquisition with mobile sensors

Here, we derive an observation operator \mathcal{B} that maps $u \in \mathcal{U}$ to measurements along a specified path. We construct \mathcal{B} in two stages. First, we impose paths with a structure via parameterization. Second, we obtain measurements by locally averaging u in neighborhoods about points on the path. This is necessary because the solution to the inversion model lies in a Sobolev space and is not necessarily defined pointwise. Having discussed this formulation, we present the properties of \mathcal{B} in Theorem 1.

We consider parameterized paths of the form $\mathbf{r} = \mathbf{r}(t; \boldsymbol{\xi})$,

$$\mathbf{r} : T_y \times \mathbb{R}^N \rightarrow \Omega, \quad (12)$$

with $T_y \subset T$. We call T_y the *inversion interval*. Given a *path parameter* $\boldsymbol{\xi} \in \mathbb{R}^N$, the parametrization $\mathbf{r}(t; \boldsymbol{\xi})$ describes the position of the sensor over the inversion interval. We assume that the partial derivatives of \mathbf{r} with respect to the path parameter exist and are continuous. Additionally, we assume the sensor performs n_y measurements of $u = \mathcal{S}m$ over T_y . Note that the choices of T_y and n_y are problem dependent.

Let $\{t_k\}_{k=1}^{n_y} \subset T_y$ be a set of measurement times and $\{\mathbf{r}_k\}_{k=1}^{n_y} := \{\mathbf{r}(t_k; \boldsymbol{\xi})\}_{k=1}^{n_y}$ be corresponding measurement locations on the path \mathbf{r} . For $k \in \{1, 2, \dots, n_y\}$, we consider the mollifier functions

$$\begin{aligned} \delta_{\mathbf{r}}(\mathbf{x}, t)(\boldsymbol{\xi}) &:= (2\pi\varepsilon_{\mathbf{x}})^{-1} \exp\left\{-\frac{\|\mathbf{x} - \mathbf{r}(t; \boldsymbol{\xi})\|_2^2}{2\varepsilon_{\mathbf{x}}}\right\}; \quad \text{and} \\ \tau_k(t) &:= (\sqrt{2\pi\varepsilon_t})^{-1} \exp\left\{-\frac{(t - t_k)^2}{2\varepsilon_t}\right\}. \end{aligned} \quad (13)$$

The constants $\varepsilon_{\mathbf{x}}, \varepsilon_t > 0$ control the scaling of the mollifiers. As these numbers tend towards zero, the mollifiers weakly converge to the delta Dirac distribution. For $\boldsymbol{\xi} \in \mathbb{R}^N$, the action of the observation operator $\mathcal{B}(\boldsymbol{\xi})$ on $u \in \mathcal{U}$ produces a vector in \mathbb{R}^{n_y} ; we define its k th component by

$$(\mathcal{B}(\boldsymbol{\xi})u)_k := \langle\langle \tau_k \delta_{\mathbf{r}}(\boldsymbol{\xi}), u \rangle\rangle, \quad k \in \{1, \dots, n_y\}. \quad (14)$$

The following result establishes the key properties of this observation operator.

Theorem 1 *The observation operator \mathcal{B} defined in (14) satisfies the following properties:*

1. if $u \in C(\Omega \times T)$, then

$$\lim_{(\varepsilon_{\mathbf{x}}, \varepsilon_t) \rightarrow (0, 0)} (\mathcal{B}(\boldsymbol{\xi})u)_k = u(\mathbf{r}_k(\boldsymbol{\xi}), t_k); \quad (15)$$

2. $\mathcal{B}(\boldsymbol{\xi}) \in \mathcal{L}(\mathcal{U}; \mathbb{R}^{n_y})$, for all $\boldsymbol{\xi} \in \mathbb{R}^N$;

3. $\mathcal{B}(\cdot) : \mathbb{R}^N \rightarrow \mathcal{L}(\mathcal{U}; \mathbb{R}^{n_y})$ is continuous in operator norm; and

4. the adjoint of \mathcal{B} , denoted by \mathcal{B}^* , satisfies

$$\mathcal{B}^*(\boldsymbol{\xi})\mathbf{y} := \delta_{\mathbf{r}}(\boldsymbol{\xi}) \sum_{k=1}^{n_y} \tau_k y_k, \quad \mathbf{y} \in \mathbb{R}^{n_y}. \quad (16)$$

Proof See Appendix A. □

Remark 1 Henceforth, the terms *design vector* and *path parameter* are interchangeable. Also, in the present setting, the observation operator depends nonlinearly on the design vector $\boldsymbol{\xi}$. Subsequently, the resulting design criteria are nonlinear and nonconvex functions of $\boldsymbol{\xi}$.

3.2 The design criterion

We define the design criterion as the posterior variance of a bounded linear functional $f : \mathcal{M} \rightarrow \mathbb{R}$. Namely,

$$\Psi := \mathbb{V}_{\mu_{\text{post}}^{\mathbf{y}, \boldsymbol{\xi}}} \{f\}. \quad (17)$$

This is motivated by a *goal-oriented* formulation [5, 10, 32], where we seek designs that minimize the uncertainty in a prediction quantity that is defined as a functional of the inversion parameter. This is in contrast to *classical* design criteria, which quantify uncertainty in the inversion parameter itself.

By the Riesz representation theorem, there exists a unique $c \in \mathcal{M}$ such that $f(m) = \langle c, m \rangle$, for all $m \in \mathcal{M}$. Recall also that $\mu_{\text{post}}^{\mathbf{y}, \boldsymbol{\xi}}$ is a Gaussian measure with mean and covariance specified in (9). Thus, $\mathbb{V}_{\mu_{\text{post}}^{\mathbf{y}, \boldsymbol{\xi}}} \{f\} = \langle \mathcal{C}_{\text{post}} c, c \rangle$, which follows directly from the definition of the posterior covariance operator; see, e.g., [1]. Since $\mathcal{C}_{\text{post}}$ is a function of the design vector, we have

$$\Psi(\boldsymbol{\xi}) = \langle \mathcal{C}_{\text{post}}(\boldsymbol{\xi}) c, c \rangle. \quad (18)$$

This is a Bayesian *c-optimality criterion*—a terminology rooted in traditional statistics literature. Specifically, in that context, one considers the posterior variance of a linear combination of finitely many scalar-valued parameters. Hence, (17) defines an infinite-dimensional c-optimality criterion. In Subsection 3.4 we provide a specific example of a c-optimality criterion used in our numerical demonstrations.

3.3 The derivatives of Ψ

The main results of this subsection are Theorem 2 and Theorem 4. These results provide formulas for the derivatives of a parameterized covariance-like operator and the path-dependent posterior covariance operator. In particular, Theorem 4 is essential for computing the gradient of Ψ (see Corollary 5) as well as other choices of path-dependent design criteria.

For $\xi \in \mathbb{R}$, let $\mathcal{H}_0(\xi) \in \mathcal{L}_{\text{sym}}^+(\mathcal{M})$ and $\mathcal{C}_0(\xi) \in \mathcal{L}_{\text{sym}}^{++}(\mathcal{M})$, where \mathcal{C}_0 is not assumed to be surjective. Hence, \mathcal{C}_0^{-1} an operator from the range of \mathcal{C}_0 to \mathcal{M} and possibly unbounded. In the case where \mathcal{C}_0 is a prior covariance operator, which is trace-class, the range of \mathcal{C}_0 is a dense subspace of \mathcal{M} and \mathcal{C}_0^{-1} is unbounded. We then consider the operator

$$\mathcal{H}(\xi) := \mathcal{H}_0(\xi) + \mathcal{C}_0^{-1}. \quad (19)$$

Note that \mathcal{H} is a self-adjoint, strictly positive, and a possibly unbounded operator defined on the range of \mathcal{C}_0 . It can be shown that the inverse $\mathcal{C} := \mathcal{H}^{-1}$ exists and for every $\xi \in \mathbb{R}$, belongs to $\mathcal{L}_{\text{sym}}^{++}(\mathcal{M})$. Here, \mathcal{C} , is an analogue of the posterior covariance operator in (9) with some assumptions relaxed.

We say that $\mathcal{C} : \mathbb{R} \rightarrow \mathcal{L}_{\text{sym}}^{++}(\mathcal{M})$ is Frechét differentiable at ξ if there exists $\mathcal{A} : \mathbb{R} \rightarrow \mathcal{L}(\mathcal{M})$ such that

$$\lim_{h \rightarrow 0} \left\| \left| \frac{\mathcal{C}(\xi + h) - \mathcal{C}(\xi)}{h} - \mathcal{A}(\xi) \right| \right\| = 0. \quad (20)$$

In this case, we write

$$\dot{\mathcal{C}}(\xi) := \mathcal{A} = \lim_{h \rightarrow 0} \frac{1}{h} (\mathcal{C}(\xi + h) - \mathcal{C}(\xi)), \quad (21)$$

where the dot above \mathcal{C} denotes derivative with respect to ξ . We use this notion of differentiability in Theorem 2—providing us with a formula for $\dot{\mathcal{C}}$.

Theorem 2 *Consider the operator $\mathcal{C} = \mathcal{H}^{-1}$ with \mathcal{H} as defined in (19). If \mathcal{H}_0 is Frechét differentiable in \mathbb{R} , then*

$$\dot{\mathcal{C}} \equiv -\mathcal{C} \dot{\mathcal{H}}_0 \mathcal{C}. \quad (22)$$

Proof See Appendix B. □

The proof of Theorem 2 is insightful and requires careful treatment of linear operators in Hilbert space.

We also need a notion of differentiability for parameterized elements of the solution space \mathcal{U} . Suppose that $u : \mathbb{R} \rightarrow \mathcal{U}$. Similar to the operator setting, we say that $u(\xi) \in \mathcal{U}$ is Frechét differentiable at ξ if there exists $a \in \mathcal{U}$ such that

$$\lim_{h \rightarrow 0} \left\| \frac{u(\xi + h) - u(\xi)}{h} - a \right\|_{\mathcal{U}} = 0. \quad (23)$$

In this case, we write

$$\dot{u} = a = \lim_{h \rightarrow 0} \frac{1}{h} (u(\xi + h) - u(\xi)). \quad (24)$$

Recall that the tensor product of $u, v \in \mathcal{U}$, denoted by $u \otimes v$, is an element of $\mathcal{L}(\mathcal{U})$, defined by $(u \otimes v)w = u\langle\langle v, w \rangle\rangle$, for all $w \in \mathcal{U}$. To find the derivatives of $\mathcal{C}_{\text{post}}$, we need to differentiate through such tensor product operators. This is facilitated by the following lemma:

Lemma 3 Suppose that $u, v : \mathbb{R} \rightarrow \mathcal{U}$ are Frechét differentiable in \mathbb{R} and define the operator $\mathcal{K} : \mathbb{R} \rightarrow \mathcal{L}(\mathcal{U})$ by $\mathcal{K}(\xi) = (u \otimes v)(\xi)$. Then, $\dot{\mathcal{K}} \equiv u \otimes \dot{v} + \dot{u} \otimes v$.

Proof We note that

$$\begin{aligned} \lim_{h \rightarrow 0} \frac{1}{h} (\mathcal{K}(\xi + h) - \mathcal{K}(\xi)) &= \lim_{h \rightarrow 0} \frac{1}{h} (u(\xi + h) \otimes v(\xi + h) - u(\xi) \otimes v(\xi)) \\ &= \lim_{h \rightarrow 0} \frac{1}{h} u(\xi + h) \otimes (v(\xi + h) - v(\xi)) + \lim_{h \rightarrow 0} \frac{1}{h} (u(\xi + h) - u(\xi)) \otimes v(\xi) \\ &= u \otimes \dot{v} + \dot{u} \otimes v. \end{aligned}$$

Here, we have also used the fact that u and v are continuous in ξ . \square

Now we have the tools needed to derive the derivatives of $\mathcal{C}_{\text{post}}(\xi)$ as stated in Theorem 4.

Theorem 4 Consider the posterior covariance operator $\mathcal{C}_{\text{post}}$ defined in (9). Then, for $\xi \in \mathbb{R}^N$ and $j \in \{1, \dots, N\}$,

$$\partial_j \mathcal{C}_{\text{post}}(\xi) = -\mathcal{C}_{\text{post}}(\xi) (\partial_j \mathcal{H}(\xi)) \mathcal{C}_{\text{post}}(\xi), \quad (25a)$$

$$\partial_j \mathcal{H}(\xi) = -\sigma^{-2} \mathcal{S}^* \left(\sum_{k=1}^{n_y} \tau_k \delta_r(\xi) \otimes \tau_k \partial_j \delta_r(\xi) + \tau_k \partial_j \delta_r(\xi) \otimes \tau_k \delta_r(\xi) \right) \mathcal{S}, \quad (25b)$$

where we define $\partial_j := \frac{\partial}{\partial \xi_j}$.

Proof Viewing $\mathcal{C}_{\text{post}}$ as a function of the j th component of ξ , we apply Theorem 2 to obtain (25a). We are then left to derive an explicit representation for $\partial_j \mathcal{H}$. The design vector appears in the operator $(\mathcal{B}^* \mathcal{B})(\xi) := [\mathcal{B}(\xi)]^* \mathcal{B}(\xi)$ and the solution operator \mathcal{S} is independent of ξ . Hence, the derivative of the Hessian is

$$\partial_j \mathcal{H}(\xi) = \sigma^{-2} \mathcal{S}^* \partial_j (\mathcal{B}^* \mathcal{B})(\xi) \mathcal{S}. \quad (26)$$

Note that for $u \in \mathcal{U}$, the definition of \mathcal{B}^* in Theorem 1 provides that

$$(\mathcal{B}^* \mathcal{B})(\xi) u = \delta_r(\xi) \sum_{k=1}^{n_y} \tau_k \langle\langle \tau_k \delta_r(\xi), u \rangle\rangle.$$

We then obtain an explicit representation of this operator with the tensor product \otimes . Specifically,

$$(\mathcal{B}^* \mathcal{B})(\xi) = \sum_{k=1}^{n_y} \tau_k \delta_r(\xi) \otimes \tau_k \delta_r(\xi)$$

Then, by invoking Lemma 3, we are left with

$$\partial_j (\mathcal{B}^* \mathcal{B})(\xi) = \sum_{k=1}^{n_y} \tau_k \delta_r(\xi) \otimes \tau_k \partial_j \delta_r(\xi) + \tau_k \partial_j \delta_r(\xi) \otimes \tau_k \delta_r(\xi). \quad (27)$$

Subsequently, (25a) follows from combining (27) with (26). \square

Using Theorem 4, we are now ready to derive the derivatives of the general c-optimality criterion:

Corollary 5 For $j \in \{1, \dots, N\}$, the j th partial derivative of the c-optimality criterion Ψ in (18) is given by

$$\partial_j \Psi(\xi) = -2\sigma^{-2} \langle \mathcal{B}(\xi) \mathcal{S} \mathcal{C}_{\text{post}}(\xi) c, (\partial_j \mathcal{B}(\xi)) \mathcal{S} \mathcal{C}_{\text{post}}(\xi) c \rangle_2. \quad (28)$$

Proof For notational convenience, we suppress dependencies on the design vector ξ in what follows. Using that $\mathcal{C}_{\text{post}}$ is self-adjoint and the identity (25a) from Theorem 4, we obtain

$$\partial_j \Psi = \langle \partial_j \mathcal{C}_{\text{post}} c, c \rangle = -\langle (\partial_j \mathcal{H}) \mathcal{C}_{\text{post}} c, \mathcal{C}_{\text{post}} c \rangle. \quad (29)$$

Then, (25b) and manipulating the tensor products reveals

$$(\partial_j \mathcal{H}) \mathcal{C}_{\text{post}} c = -\sigma^{-2} \sum_{k=1}^{n_y} \langle \tau_k \partial_j \delta_r, \mathcal{S} \mathcal{C}_{\text{post}} c \rangle \mathcal{S}^* \tau_k \delta_r + \langle \tau_k \delta_r, \mathcal{S} \mathcal{C}_{\text{post}} c \rangle \mathcal{S}^* \tau_k \partial_j \delta_r.$$

We then substitute this expression back into (29) and use properties of the inner product to obtain

$$\partial_j \Psi = -2\sigma^{-2} \sum_{k=1}^{n_y} \langle \tau_k \delta_r, \mathcal{S} \mathcal{C}_{\text{post}} c \rangle \langle \tau_k \partial_j \delta_r, \mathcal{S} \mathcal{C}_{\text{post}} c \rangle.$$

Denoting the k th component of $\mathcal{B} \mathcal{S} \mathcal{C}_{\text{post}} c$ and $(\partial_j \mathcal{B}) \mathcal{S} \mathcal{C}_{\text{post}} c$ by $[\mathcal{B} \mathcal{S} \mathcal{C}_{\text{post}} c]_k$ and $[(\partial_j \mathcal{B}) \mathcal{S} \mathcal{C}_{\text{post}} c]_k$, respectively,

$$\begin{aligned} \langle \tau_k \delta_r, \mathcal{S} \mathcal{C}_{\text{post}} c \rangle &= [\mathcal{B} \mathcal{S} \mathcal{C}_{\text{post}} c]_k, \\ \langle \tau_k \partial_j \delta_r, \mathcal{S} \mathcal{C}_{\text{post}} c \rangle &= [(\partial_j \mathcal{B}) \mathcal{S} \mathcal{C}_{\text{post}} c]_k. \end{aligned} \quad (30)$$

Recalling (28), the proof is concluded since

$$\partial_j \Psi = -2\sigma^{-2} \sum_{k=1}^{n_y} [\mathcal{B} \mathcal{S} \mathcal{C}_{\text{post}} c]_k [(\partial_j \mathcal{B}) \mathcal{S} \mathcal{C}_{\text{post}} c]_k.$$

□

We remark that the formula for $\partial_j \Psi$ presented in Corollary 5 holds for every $c \in \mathcal{M}$. In the following subsection, we specify the c-optimality criterion and its gradient for a certain c .

3.4 A specific criterion

Here we present the c-optimality criterion used in our numerical demonstrations; see Section 6. In particular, we consider a certain bounded linear functional of m , referred to as a *goal-functional*, which represents a prediction or quantity of interest. Having derived the vector $c \in \mathcal{M}$ which characterizes this goal-functional, we specialize the formulas for the criterion and its derivatives.

Let $v \in \mathcal{U}$ and consider the goal-functional $Z : \mathcal{M} \rightarrow \mathbb{R}$ defined by

$$Z(m) := \langle v, \mathcal{S}m \rangle, \quad m \in \mathcal{M}. \quad (31)$$

If v is an indicator function of a spatio-temporal subdomain of $\Omega \times T$, then Z is a random variable describing the integration of the solution $u = \mathcal{S}m$ over this subdomain. The resulting optimality criterion is then

$$\Psi(\xi) := \mathbb{V}_{\mu_{\text{post}}^{y, \xi}} \{Z\}. \quad (32)$$

Using the adjoint of \mathcal{S} , an equivalent characterization of the goal-functional is $Z(m) = \langle \mathcal{S}^* v, m \rangle$. Hence, Ψ is the c-optimality criterion in (18) with $c = \mathcal{S}^* v$. Equivalently,

$$\Psi(\xi) = \langle \mathcal{C}_{\text{post}}(\xi) \mathcal{S}^* v, \mathcal{S}^* v \rangle. \quad (33)$$

We can also substitute $c = \mathcal{S}^* v$ in the derivative formula (28), providing

$$\partial_j \Psi = -2\sigma^{-2} \langle \mathcal{B}(\xi) \mathcal{S} \mathcal{C}_{\text{post}}(\xi) \mathcal{S}^* v, (\partial_j \mathcal{B}(\xi)) \mathcal{S} \mathcal{C}_{\text{post}}(\xi) \mathcal{S}^* v \rangle_2. \quad (34)$$

Remark 2 The above developments extend naturally to other optimality criteria in the infinite-dimensional setting. In particular, the A- and D-optimality criteria emerge in a straightforward manner. We recall that the A-optimality criterion [1] is defined by $\Psi_A := \text{tr}(\mathcal{C}_{\text{post}})$, which can be approximated using a Monte Carlo trace estimator. The formula for the partial derivative of Ψ in Corollary 5 can then be used to compute the gradient of trace-estimated A-optimality criterion. The D-optimality criterion [2] is also within reach. Evaluating this criterion requires computing the spectrum of the *prior-preconditioned data misfit Hessian* $\mathcal{C}_{\text{pr}}^{1/2} \mathcal{H}_{\text{mis}} \mathcal{C}_{\text{pr}}^{1/2}$, which we already do in our numerical implementation; see Subsection 5.4.

4 Parameterized sensor paths

Our framework is compatible with any parameterized curve $\mathbf{r}(\cdot; \boldsymbol{\xi}) \in \mathbb{R}^2$ that is continuously differentiable with respect to the path parameter $\boldsymbol{\xi}$, and it readily extends to three-dimensional domains. The specific form of parameterization depends on problem-specific factors related to the inversion model and sensor apparatus. For example, an aerial drone has a limited battery life and capability to accelerate—both influential on the choice of parameterization or constraints on $\boldsymbol{\xi}$. We present two flexible parameterizations: *Bézier* and *Fourier* paths. After defining these path types in Subsection 4.1, we show how constraints and other practical considerations can be incorporated in the path-OED problem in Subsection 4.2.

4.1 Path types

In this subsection, we discuss Bézier and Fourier paths for path-OED.

Bézier curves. Bézier curves [16, 17] are commonly used in computer graphics, approximation theory, and optimization. Such curves have been utilized in optimal path-planning as well. In particular, Bézier curves were used to solve an autonomous vehicle path-planning problem in [35], where the path is constrained to a corridor. Bézier curves are also utilized in optimal control literature; see e.g., [25, 29]. The existing theory and software for Bézier curves make them a natural choice for parameterizing sensor trajectories.

A degree N_b Bézier curve is a polynomial of degree N_b that is uniquely characterized by a set of *control points* $\{\mathbf{p}_j\}_{j=0}^{N_b} \subset \mathbb{R}^2$. The Bézier curve corresponding to this set of control points is

$$\mathbf{r}_b(t; \boldsymbol{\xi}_b) := \sum_{j=0}^{N_b} \binom{N_b}{j} t^j (1-t)^{N_b-j} \mathbf{p}_j, \quad t \in [0, 1], \quad (35)$$

where $\boldsymbol{\xi}_b := [\mathbf{p}_0^\top \ \mathbf{p}_1^\top \ \cdots \ \mathbf{p}_{N_b}^\top]^\top \in \mathbb{R}^{2(N_b+1)}$. We use (35) to describe the path of a mobile sensor. While the formula for \mathbf{r}_b is defined over $t \in [0, 1]$, we can use a linear change of variable to define \mathbf{r}_b over the inversion interval T_y . The first and last control points specify the endpoints of the Bézier curve. If these points coincide, then the curve is closed. Intermediate control points do not necessarily lie on the curve, but have the behavior of attracting the curve in the direction of the control points. We depict two Bézier curves in Figure 1.

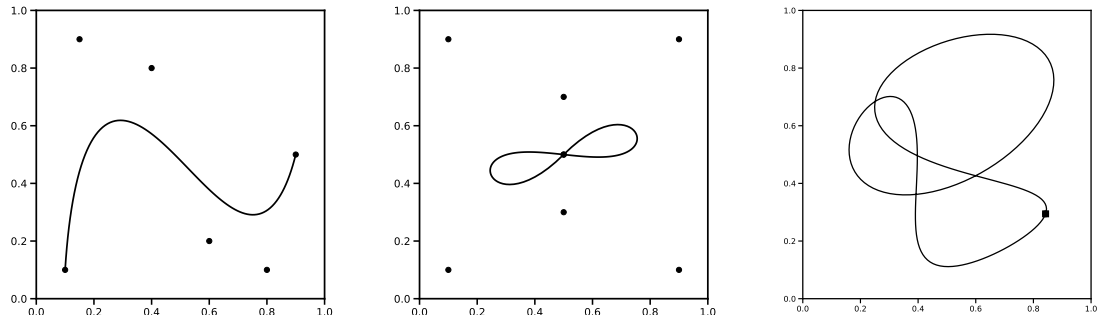


Fig. 1: Left and Middle: Bézier curves of degree $N_b = 5$ with control points plotted as dots. Right: A Fourier path with $N_f = 3$ modes.

Fourier paths. Let $\bar{\mathbf{x}} \in \Omega$ and $N_f \in \mathbb{N}$. Given $t \in T_y$ and a set of N_f frequencies $\{\omega_j\}_{j=1}^{N_f}$, the Fourier path \mathbf{r}_f with N_f modes is defined by

$$\mathbf{r}_f(t; \boldsymbol{\xi}_f) := \bar{\mathbf{x}} + \sum_{j=1}^{N_f} \begin{bmatrix} a_j \cos(\omega_j t) + b_j \sin(\omega_j t) \\ c_j \cos(\omega_j t) + d_j \sin(\omega_j t) \end{bmatrix}, \quad (36)$$

where $\boldsymbol{\xi}_f := [a_1 \ b_1 \ c_1 \ d_1 \ \dots \ a_{N_f} \ b_{N_f} \ c_{N_f} \ d_{N_f}]^\top \in \mathbb{R}^{4N_f}$. For a path $\mathbf{r}(t) : \mathbb{R} \rightarrow \mathbb{R}^2$ whose components lie in the space $L^2(T_y)$, the Fourier basis

$$\{\cos(\omega_j t), \sin(\omega_j t)\}_{j=0}^{\infty} \quad \text{with} \quad \omega_j := \frac{2\pi j}{|T_y|}, \quad (37)$$

can be used to approximate each component of \mathbf{r} . This motivates the representation in (36). We illustrate an example of a Fourier path in Figure 1.

Note that the summation term in (36) is a linear transformation of the path parameter (design vector). Thus, \mathbf{r}_f can be viewed as an affine transformation on $\boldsymbol{\xi}_f$, parameterized over T_y . The shift term $\bar{\mathbf{x}}$ accounts for the constant basis function in (37). We use this to translate the path into Ω . Fourier paths are periodic and can generate a rich family of curves, even with a low number of modes.

4.2 Imposing physical constraints

Here, we discuss the following practical considerations (i) confining sensor paths to Ω ; (ii) regularizing penalty terms; and (iii) incorporating regions where data are known to be obscured.

Confining paths. In many applications we want to keep the sensor in the domain Ω . One way of enforcing this is to place a constraint directly on the path parameter $\boldsymbol{\xi}$. In the case of Bézier paths, it is known that the curve \mathbf{r}_b lies in the convex hull of its control points [35]. Thus, in the case of a convex domain Ω , we can keep the Bézier path in Ω by restricting the control points to Ω . In the case that Ω is rectangular, enforcing this constraint results in an optimization problem with a linear inequality constraint on $\boldsymbol{\xi}_b$.

Confining \mathbf{r}_f to Ω is not as simple. One idea is to constrain \mathbf{r}_f to a box about $\bar{\mathbf{x}}$. Choose $\tilde{\mathbf{x}} \in \mathbb{R}_+^2$ such that

$$[\bar{x}_1 - \tilde{x}_1, \bar{x}_1 + \tilde{x}_1] \times [\bar{x}_2 - \tilde{x}_2, \bar{x}_2 + \tilde{x}_2] \subseteq \Omega. \quad (38)$$

Without loss of generality, focusing on the first component of \mathbf{r}_f in (36), the triangle inequality provides

$$\left| \sum_{j=1}^{N_f} a_j \cos(\omega_j t) + b_j \sin(\omega_j t) \right| \leq \sum_{j=1}^{N_f} |a_j| + |b_j|.$$

Thus, we can confine \mathbf{r}_f to the box (38) by enforcing

$$\sum_{j=1}^{N_f} \begin{bmatrix} |a_j| + |b_j| \\ |c_j| + |d_j| \end{bmatrix} \leq \begin{bmatrix} \tilde{x}_1 \\ \tilde{x}_2 \end{bmatrix}. \quad (39)$$

We note that this is a nonlinear constraint on $\boldsymbol{\xi}_f$ and that (39) is satisfied whenever

$$|a_j|, |b_j| \leq \frac{\tilde{x}_1}{2N_f} \quad \text{and} \quad |c_j|, |d_j| \leq \frac{\tilde{x}_2}{2N_f}, \quad j \in \{1, 2, \dots, N_f\}. \quad (40)$$

Hence, (40) is a linear constraint that confines the Fourier paths to a box about $\bar{\mathbf{x}}$. Unfortunately, this is conservative. A constraint that allows the paths to explore the domain more freely is desirable. The following result provides a simple nonlinear constraint that confines the sensor path to a circular subdomain of Ω .

Theorem 6 Let $R_\Omega > 0$ and consider the Fourier path \mathbf{r}_f in (36). We have,

$$\|\mathbf{r}_f - \bar{\mathbf{x}}\|_2 \leq R_\Omega, \quad \text{whenever} \quad \|\boldsymbol{\xi}_f\|_2 \leq \frac{R_\Omega}{\sqrt{N_f}}.$$

Proof See Appendix D. □

Remark 3 In the proof of Theorem 6 we use the affine structure of the Fourier path type. In fact, we can derive a constraint on the design vector that allows us to restrict any affine path to a disk of radius R_Ω . Specifically, let $\mathbf{T} : T_y \rightarrow \mathbb{R}^{2 \times N}$ and consider a path of the form $\mathbf{r}(t; \boldsymbol{\xi}) = \bar{\mathbf{x}} + \mathbf{T}(t)\boldsymbol{\xi}$. Then, for any $\boldsymbol{\xi} \in \mathbb{R}^N$ and $\bar{\mathbf{x}} \in \mathbb{R}^2$,

$$\|\mathbf{r}(t; \boldsymbol{\xi}) - \bar{\mathbf{x}}\|_2 = \|\mathbf{T}(t)\boldsymbol{\xi}\| \leq \|\mathbf{T}(t)\|_2 \|\boldsymbol{\xi}\|_2 \leq \|\boldsymbol{\xi}\|_2 \sup_{t \in T_y} \|\mathbf{T}(t)\|_2.$$

Hence,

$$\|\mathbf{r} - \bar{\mathbf{x}}\|_2 \leq R_\Omega, \quad \text{whenever} \quad \|\boldsymbol{\xi}\|_2 \leq \frac{R_\Omega}{\sup_{t \in T_y} \|\mathbf{T}(t)\|_2}. \quad (41)$$

For certain parameterizations, numerically computing the supremum of $\|\mathbf{T}(t)\|_2$ over the inversion interval can be expensive. An advantage of the Fourier path type is that we can compute $\|\mathbf{T}(t)\|_2$ analytically. Specifically, we can show that $\|\mathbf{T}(t)\|_2 = \sqrt{N_f}$ for all $t \in T_y$; see Theorem 6.

Penalizing acceleration. A common issue for solutions to the optimal path problem are curves with sharp turns or kinks. One method for preventing this is to include a penalty term in the optimization problem. We propose regularizing the optimality criterion Ψ by adding the following term:

$$R(\boldsymbol{\xi}; \gamma) := \frac{\gamma}{2} \int_{T_y} \|\ddot{\mathbf{r}}(t; \boldsymbol{\xi})\|_2^2 dt. \quad (42)$$

This characterizes the time-integrated magnitude of the path's acceleration. Hence, regularizing with R will result in smoother optimal paths. In practice, we find it necessary to penalize the Fourier paths in this manner. The penalty R for the Fourier path is computed to be

$$R(\boldsymbol{\xi}_f; \gamma) = \frac{\gamma|T_y|}{4} \sum_{j=1}^{N_f} \omega_j^4 (a_j^2 + b_j^2 + c_j^2 + d_j^2). \quad (43)$$

On the other hand, the regularity of the Bézier paths can be easily controlled by modulating the number of control points. In this case, adding such regularizing penalty terms were not needed.

Obscured regions. In some applications, there may be a subdomain of Ω where the state u is concealed or data is otherwise challenging to collect. We refer to such areas as *obscured regions*. Our motivation of considering such regions stems from wildfire applications, where smoke or other obstacles might degrade the ability of a sensor to collect data. However, we assume that the sensor is not necessarily prohibited, but rather discouraged, from entering such obscured regions.

We explain how to incorporate a disk-shaped obscured region into the path-OED problem. Namely, let $\mathbf{x}_D \in \Omega$ and $R_D > 0$. Then, we define the obscured region $D \subset \Omega$ by

$$D := \{\mathbf{x} \in \Omega : \|\mathbf{x} - \mathbf{x}_D\|_2 \leq R_D\}. \quad (44)$$

It is possible to force the sensor path to avoid D completely by incorporating a hard constraint in the path-OED formulation. However, this adds complexity to the optimization problem. Here, we outline a tractable approach for discouraging data-acquisition within D that avoids such hard constraints. The key idea is to artificially modulate the noise variance of the data model, filtering-out observations that occur within D . A challenge with this approach is preserving the differentiability of $\mathcal{C}_{\text{post}}(\boldsymbol{\xi})$.

We consider a smoothed indicator function for D , denoted by p . For $\beta > 0$, we define this function by

$$p(\mathbf{x}) := \left(1 + \exp \left\{ \frac{\|\mathbf{x} - \mathbf{x}_D\|_2 - R_D}{\beta} \right\} \right)^{-1}, \quad \mathbf{x} \in \Omega. \quad (45)$$

We note that (45) is type of radial basis function (RBF) [8] and remark on a few of its properties. For a sufficiently small β and $\mathbf{x} \in D$, we have that $p(\mathbf{x}) \approx 1$. Similarly, $p(\mathbf{x}) \approx 0$ for $\mathbf{x} \notin D$. The parameter β controls the steepness of the transition region—a small β resulting in a closer approximation to an indicator function. The RBF p is depicted for various scaling parameters in Figure 2. We can extend the present framework for obscured regions to more complex geometries by considering linear combinations of RBFs. Namely, we can approximate obscured regions that are not disks by summing RBFs.

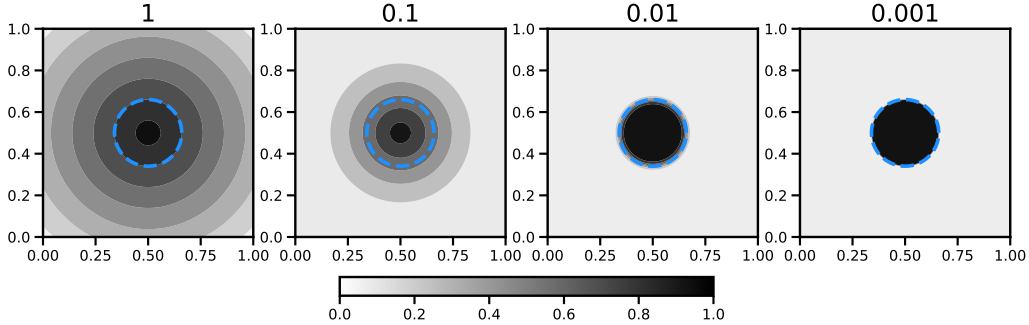


Fig. 2: Contours of the RBF p with $\mathbf{x}_D = (0.5, 0.5)$, $R_D = 0.16$, and $\beta \in \{1, 0.1, 0.01, 0.001\}$. The dotted blue circle represents the boundary of the obscured region.

Consider the data-misfit Hessian $\mathcal{H}_{\text{mis}}(\xi)$ in (11) for a given ξ . This operator can be expressed as $\mathcal{H}_{\text{mis}}(\xi) = \mathcal{F}^*(\xi)(\sigma^{-2}\mathbf{I})\mathcal{F}(\xi)$. This indicates that the noise covariance matrix $\sigma^2\mathbf{I}$ (and its inverse) has the role of *filtering* or weighting observations. We extend this idea by smoothly modulating contributions of measurements locations based on their position relative to D .

Consider n_y measurement times $\{t_k\}_{k=1}^{n_y}$, and for a path \mathbf{r} , define $\mathbf{p} : \mathbb{R}^N \rightarrow (0, 1)^{n_y}$ by

$$p_k(\xi) := p(\mathbf{r}(t_k; \xi)), \quad k \in \{1, 2, \dots, n_y\}. \quad (46)$$

Subsequently, we form the diagonal weighting matrix $\mathbf{P} : \mathbb{R}^N \rightarrow \mathbb{R}^{n_y \times n_y}$ defined by

$$\mathbf{P}(\xi) := \text{diag}(p_1(\xi), \dots, p_{n_y}(\xi)). \quad (47)$$

This is inserted into $\mathcal{H}_{\text{mis}}(\xi)$, resulting in the “filtered Hessian”:

$$\mathcal{H}_{\mathcal{D}}(\xi) := \sigma^{-2}\mathcal{F}^*(\xi)(\mathbf{I} - \mathbf{P}(\xi))\mathcal{F}(\xi) + \mathcal{C}_{\text{pr}}^{-1}. \quad (48)$$

Using the matrix $\mathbf{I} - \mathbf{P}(\xi)$ in (48) filters out observations that occur in the obscured region. In practice, we solve the path-OED problem using the filtered Hessian (and posterior covariance), then discard the measurements in D when solving the inverse problem. We derive the derivative of the filtered criterion Ψ as in (33) in Appendix C. The resulting formula for $\partial_j \Psi$ contains the gradient of p . This is given by

$$\nabla p = -\frac{\mathbf{x}p^2}{\beta\|\mathbf{x} - \mathbf{x}_D\|_2} \exp \left\{ \frac{\|\mathbf{x} - \mathbf{x}_D\|_2 - R_D}{\beta} \right\}. \quad (49)$$

The effectiveness of the present filtered approach for incorporating obscured regions is illustrated in our numerical results in Section 6.

5 Solving the discretized path-OED problem

In this section, we describe how to discretize and solve the path-OED problem. The developments here lay the foundations for an efficient computational framework. First, we construct finite-dimensional analogues for the parameter space \mathcal{M} and solution space \mathcal{U} ; see Subsection 5.1. Then, we discretize the inverse problem in Subsection 5.2. Subsequently, we discuss the discretized version of the path-OED problem in Subsection 5.3. In that subsection, we derive the discretized c-optimality criterion and its gradient, and specialize the results to the specific criterion considered in Subsection 3.4. Lastly, we discuss computational considerations in Subsection 5.4, where we measure computational cost in terms of applications of the solution operator.

5.1 Structure of the discretized Hilbert spaces

We let $\{t_\ell\}_{\ell=0}^{n_t} \subset T$ be the *global time discretization* and consider n_y measurement times occurring during the inversion interval T_y . For convenience, we assume equidistant time steps. That is, $t_{\ell+1} - t_\ell = \Delta t$, for $\ell \in \{0, 1, \dots, n_t - 1\}$, where Δt is a fixed step size. In principle, the measurement times are independent of this discretization. However, for simplicity, we assume they occur at some subset of the global temporal discretization. Specifically, we denote the measurement times by $\{t_{\ell_k}\}_{k=1}^{n_y} \subset T_y$. This setup can be interpreted as having a sampling frequency that is a multiple of a fixed global time step.

For spatial discretization, we use the continuous Galerkin finite element method. Let $\{\phi_i\}_{i=1}^{n_x}$ be a nodal finite element basis consisting of compactly supported functions. Then, $m \in \mathcal{M}$ admits the approximation

$$m_h(\mathbf{x}) := \sum_{i=1}^{n_x} m_i \phi_i(\mathbf{x}) \quad (50)$$

and we identify m_h with the coefficient vector $\mathbf{m} := [m_1 \ m_2 \ \dots \ m_{n_x}]^\top$. Subsequently, for $c \in \mathcal{M}$ with finite element approximation c_h , we estimate the inner product $\langle m, c \rangle$ with the calculation

$$\langle m_h, c_h \rangle = \int_{\Omega} m_h c_h \, d\mathbf{x} = \sum_{i,j=1}^{n_x} m_i c_j \langle \phi_i, \phi_j \rangle.$$

This motivates the *mass-weighted* inner product space $\mathbb{R}_{\mathbf{M}}^{n_x}$. Specifically, we define the *mass matrix* \mathbf{M} by $M_{ij} := \langle \phi_i, \phi_j \rangle$, for $i, j \in \{1, \dots, n_x\}$. Then, for $\mathbf{m}, \mathbf{c} \in \mathbb{R}_{\mathbf{M}}^{n_x}$, the inner product on $\mathbb{R}_{\mathbf{M}}^{n_x}$ is defined by

$$\langle \mathbf{m}, \mathbf{c} \rangle_{\mathbf{M}} := \mathbf{m}^\top \mathbf{M} \mathbf{c}. \quad (51)$$

We use a similar strategy to discretize \mathcal{U} . Let $u \in \mathcal{U}$ and define the spatial approximation u_h of u by

$$u_h(\mathbf{x}, t) := \sum_{i=1}^{n_x} u_i(t) \phi_i(\mathbf{x}). \quad (52)$$

We identify u_h with the time-dependent coefficient vector $\mathbf{u}(t)$, where $\mathbf{u}(t) \in \mathbb{R}_{\mathbf{M}}^{n_x}$, for any $t \in T$. Next, we define $\mathbf{u}_\ell := \mathbf{u}(t_\ell)$, for $\ell \in \{1, \dots, n_t\}$, and form a *snapshot matrix* $\mathbf{U} := [\mathbf{u}_1 \ \dots \ \mathbf{u}_{n_t}]$ of dimension $n_x \times n_t$. Thus, for $v \in \mathcal{U}$ with approximation v_h , we estimate the inner product $\langle\langle u, v \rangle\rangle$ with

$$\langle\langle u_h, v_h \rangle\rangle = \int_T \left(\int_{\Omega} u_h v_h \, d\mathbf{x} \right) dt = \int_T \langle \mathbf{u}(t), \mathbf{v}(t) \rangle_{\mathbf{M}} dt.$$

We obtain an inner product on the space of snapshot matrices by approximating the resulting integral via numerical quadrature. Specifically, let $\mathbf{w} \in \mathbb{R}^{n_t}$ denote a vector of positive quadrature weights and let $\mathbf{V} := [\mathbf{v}_1 \ \dots \ \mathbf{v}_{n_t}]$ be the snapshot matrix corresponding to v_h . Then, the inner product is

$$\langle\langle \mathbf{U}, \mathbf{V} \rangle\rangle_{\mathbf{M}} := \sum_{\ell=1}^{n_t} w_\ell \langle \mathbf{u}_\ell, \mathbf{v}_\ell \rangle_{\mathbf{M}}. \quad (53)$$

It is straightforward to show that (53) defines an inner product on $\mathbb{R}^{n_x \times n_t}$; we denote this inner product space by $\mathbb{R}_M^{n_x \times n_t}$. In Lemma 7, we present two useful identities for (53). Specifically, we require (54a) to derive the adjoint of the discretized observation operator. In what follows, $\mathbf{U} \odot \mathbf{V}$ denotes the Hadamard product of matrices \mathbf{U} and \mathbf{V} . Specifically, for matrices of the same dimension, $(\mathbf{U} \odot \mathbf{V})_{i\ell} := U_{i\ell} V_{i\ell}$.

Lemma 7 Consider (53) and let $\mathbf{U}, \mathbf{V} \in \mathbb{R}_M^{n_x \times n_t}$. Then,

$$\langle\langle \mathbf{U}, \mathbf{V} \rangle\rangle_M = \mathbf{1}^\top (\mathbf{U} \odot \mathbf{M}\mathbf{V}) \mathbf{w} \quad (54a)$$

$$= \text{tr}(\mathbf{U}^\top \mathbf{M}\mathbf{V}\mathbf{W}), \quad (54b)$$

where $\mathbf{W} := \text{diag}(\mathbf{w})$ and $\mathbf{1} \in \mathbb{R}^{n_x}$ is a constant ones vector.

Proof We first note that $\langle \mathbf{u}_\ell, \mathbf{v}_\ell \rangle_M = \mathbf{1}^\top (\mathbf{u}_\ell \odot (\mathbf{M}\mathbf{v}_\ell))$. Subsequently, the first identity follows from

$$\sum_{\ell=1}^{n_t} w_\ell \langle \mathbf{u}_\ell, \mathbf{v}_\ell \rangle_M = \sum_{\ell=1}^{n_t} w_\ell \mathbf{1}^\top (\mathbf{u}_\ell \odot (\mathbf{M}\mathbf{v}_\ell)) = \mathbf{1}^\top \sum_{\ell=1}^{n_t} w_\ell (\mathbf{u}_\ell \odot (\mathbf{M}\mathbf{V})_\ell) = \mathbf{1}^\top (\mathbf{U} \odot \mathbf{M}\mathbf{V}) \mathbf{w}.$$

As for the second identity, we note

$$\text{tr}(\mathbf{U}^\top \mathbf{M}\mathbf{V}\mathbf{W}) = \sum_{i=1}^{n_x} \sum_{\ell=1}^{n_t} U_{i\ell} (\mathbf{M}\mathbf{V}\mathbf{W})_{i\ell} = \sum_{\ell=1}^{n_t} w_\ell \sum_{i=1}^{n_x} U_{i\ell} (\mathbf{M}\mathbf{V})_{i\ell} = \sum_{\ell=1}^{n_t} w_\ell \langle \mathbf{u}_\ell, \mathbf{v}_\ell \rangle_M.$$

□

Remark 4 Lemma 7 shows that the $\mathbb{R}_M^{n_x \times n_t}$ inner product can be viewed as a weighted Frobenius inner product. Recall that the Frobenius inner product [21, Chapter 5.2] of matrices \mathbf{A}_1 and \mathbf{A}_2 (for which $\mathbf{A}_1^\top \mathbf{A}_2$ is well-defined) is

$$\langle \mathbf{A}_1, \mathbf{A}_2 \rangle_F := \text{tr}(\mathbf{A}_1^\top \mathbf{A}_2) = \sum_{i,j} A_{ij} B_{ij}. \quad (55)$$

Now, consider $\mathbf{U}, \mathbf{V} \in \mathbb{R}_M^{n_x \times n_t}$. By Lemma 7, $\langle\langle \mathbf{U}, \mathbf{V} \rangle\rangle_M = \text{tr}(\mathbf{U}^\top \mathbf{M}\mathbf{V}\mathbf{W}) = \langle \mathbf{U}, \mathbf{M}\mathbf{V}\mathbf{W} \rangle_F$. Hence, $\langle\langle \cdot, \cdot \rangle\rangle_M$ is a Frobenius inner product that is weighted according to the spatiotemporal discretization.

5.2 The discretized inverse problem

In what follows we derive the discretized version of the inverse problem presented in Section 2. We first discuss the discrete solution and observation operators. A key result is Proposition 8, which provides the adjoint of the discretized observation operator. Subsequently, we provide formulas for the posterior mean and covariance operator associated with the finite element coefficients of the discretized inversion parameter.

The solution and observation operators. The discretized solution operator is denoted by

$$\mathbf{S} : \mathbb{R}_M^{n_x} \rightarrow \mathbb{R}_M^{n_x \times n_t}. \quad (56)$$

This linear operator maps coefficient vectors in $\mathbb{R}_M^{n_x}$ to snapshot matrices in $\mathbb{R}_M^{n_x \times n_t}$. The adjoint of the solution operator is denoted by $\mathbf{S}^* : \mathbb{R}_M^{n_x \times n_t} \rightarrow \mathbb{R}_M^{n_x}$. In Appendix E, we derive the discretized solution operator and its adjoint for the model used in our numerical experiments.

Next, we construct the discretized observation operator

$$\mathbf{B} : \mathbb{R}_M^{n_x \times n_t} \rightarrow \mathbb{R}^{n_y}. \quad (57)$$

We proceed in two steps. First, we describe how to obtain pointwise measurements of the finite element approximation u_h at all times in the discretization $\{t_\ell\}_{\ell=1}^{n_t} \subset T$. Then, we define an operator that restricts these evaluations to the measurement times $\{t_{\ell_k}\}_{k=1}^{n_y} \subset T_y$. Combining these operations together produces the action of the observation operator.

For a time t_ℓ in the global discretization of T and a path \mathbf{r} , we define $\phi_\ell : \mathbb{R}^N \rightarrow \mathbb{R}^{n_x}$ by

$$\phi_\ell(\xi) := [\phi_1(\mathbf{r}_\ell) \phi_2(\mathbf{r}_\ell) \cdots \phi_{n_x}(\mathbf{r}_\ell)]^\top, \quad \text{where } \mathbf{r}_\ell := \mathbf{r}(t_\ell; \xi). \quad (58)$$

Note that ϕ_ℓ consists of basis functions evaluated at $\mathbf{r}_\ell \in \Omega$. For an approximation m_h of $m \in \mathcal{M}$ with coefficients $\mathbf{m} \in \mathbb{R}_{\mathbf{M}}^{n_x}$, a measurement of m at \mathbf{r}_ℓ can be estimated by $\langle \mathbf{m}, \phi_\ell \rangle_2$. To see this, note that $\langle \delta_r(t_\ell; \xi), m \rangle \approx m_h(\mathbf{r}_\ell) = \sum_{i=1}^{n_x} m_i \phi_i(\mathbf{r}_\ell)$. Similarly, if u_h is the finite element approximation of $u \in \mathcal{U}$ with associated snapshot matrix $\mathbf{U} \in \mathbb{R}_{\mathbf{M}}^{n_x \times n_t}$, then a pointwise measurement of u at $(\mathbf{r}_\ell, t_\ell)$ can be estimated by $\langle \mathbf{u}_\ell, \phi_\ell \rangle_2$. Subsequently, we form the matrix $\Phi : \mathbb{R}^N \rightarrow \mathbb{R}^{n_x \times n_t}$, defined by

$$\Phi(\xi) := [\phi_1(\xi) \ \phi_2(\xi) \ \cdots \ \phi_{n_t}(\xi)]. \quad (59)$$

Using Φ , we observe the columns of \mathbf{U} at the points $\{(\mathbf{r}_\ell, t_\ell)\}_{\ell=1}^{n_t}$ via the calculation

$$(\mathbf{U} \odot \Phi(\xi))^\top \mathbf{1} = [u_h(\mathbf{r}_1, t_1) \ u_h(\mathbf{r}_2, t_2) \ \cdots \ u_h(\mathbf{r}_{n_t}, t_{n_t})]^\top. \quad (60)$$

The operation in (60) produces a measurement vector of length n_t . Hence, the final step in constructing \mathbf{B} is to discard measurements that do not occur at the times $\{t_{\ell_k}\}_{k=1}^{n_y}$. For this, we require an *extraction operator*. Let $\mathbf{e}_\ell \in \mathbb{R}^{n_t}$ be the ℓ th standard Euclidean basis vector and define $\mathbf{E} \in \mathbb{R}^{n_t \times n_y}$ by $\mathbf{E} := [\mathbf{e}_{\ell_1} \ \mathbf{e}_{\ell_2} \ \cdots \ \mathbf{e}_{\ell_{n_y}}]$. Then, the extraction operator $\mathcal{E} : \mathbb{R}^{n_x \times n_t} \rightarrow \mathbb{R}^{n_x \times n_y}$ is

$$\mathcal{E}\mathbf{U} := \mathbf{U}\mathbf{E}, \quad \mathbf{U} \in \mathbb{R}_{\mathbf{M}}^{n_x \times n_t}. \quad (61)$$

It is straightforward to show that right-multiplying \mathbf{U} by \mathbf{E} yields a matrix in $\mathbb{R}^{n_x \times n_y}$ whose columns are those of \mathbf{U} indexed by the set $\{\ell_k\}_{k=1}^{n_y}$. By combining (60) and (61), the action of \mathbf{B} on \mathbf{U} is defined by

$$\mathbf{B}(\xi)\mathbf{U} := (\mathcal{E}\mathbf{U} \odot \mathcal{E}\Phi(\xi))^\top \mathbf{1}. \quad (62)$$

To formulate the discretized inverse problem we need the adjoint operator $\mathbf{B}^* : \mathbb{R}^{n_y} \rightarrow \mathbb{R}_{\mathbf{M}}^{n_x \times n_t}$. The following proposition provides a formula for \mathbf{B}^* and enables matrix-free implementations.

Proposition 8 *Let $\mathbf{U} \in \mathbb{R}_{\mathbf{M}}^{n_x \times n_t}$, $\xi \in \mathbb{R}^N$, and define $\mathbf{w}^{-1} \in \mathbb{R}^{n_t}$ by $(\mathbf{w}^{-1})_\ell := 1/w_\ell$, for $\ell \in \{1, 2, \dots, n_t\}$. Then, the adjoint of $\mathbf{B}(\xi)$ is given by*

$$\mathbf{B}(\xi)^* \mathbf{y} = \mathbf{M}^{-1} \Phi(\xi) \text{diag}\{\mathbf{E}\mathbf{y} \odot \mathbf{w}^{-1}\}, \quad \text{for } \mathbf{y} \in \mathbb{R}^{n_y}. \quad (63)$$

Proof In what follows, we denote the ℓ th column of a matrix \mathbf{A} by $\mathbf{A}_{*,\ell}$. Moreover, since the dependence of \mathbf{B} on ξ does not play a role here, for simplicity, we suppress ξ .

Note that by the definition of the extraction operator,

$$\mathcal{E}\mathbf{U} \odot \mathcal{E}\Phi = \mathcal{E}(\Phi \odot \mathbf{U}).$$

Thus, by (62), we have the identity

$$\mathbf{B}\mathbf{U} = \mathbf{E}^\top (\mathbf{U} \odot \Phi)^\top \mathbf{1}. \quad (64)$$

Using (64) and writing the matrix-vector product $(\mathbf{U} \odot \Phi)\mathbf{E}\mathbf{y}$ as a sum, we have

$$\langle \mathbf{B}\mathbf{U}, \mathbf{y} \rangle_2 = \mathbf{1}^\top (\mathbf{U} \odot \Phi)\mathbf{E}\mathbf{y} = \mathbf{1}^\top \sum_{\ell=1}^{n_t} (\mathbf{E}\mathbf{y})_\ell (\mathbf{U} \odot \Phi)_{*,\ell}.$$

It follows directly from the definition of the Hadamard product that $(\mathbf{U} \odot \Phi)_{*,\ell} = \mathbf{u}_\ell \odot \Phi_{*,\ell}$. Thus,

$$\mathbf{1}^\top \sum_{\ell=1}^{n_t} (\mathbf{E}\mathbf{y})_\ell (\mathbf{U} \odot \Phi)_{*,\ell} = \mathbf{1}^\top \sum_{\ell=1}^{n_t} (\mathbf{E}\mathbf{y})_\ell (\mathbf{u}_\ell \odot \Phi_{*,\ell}) = \mathbf{1}^\top \sum_{\ell=1}^{n_t} w_\ell \mathbf{u}_\ell \odot \left(\frac{(\mathbf{E}\mathbf{y})_\ell}{w_\ell} \Phi_{*,\ell} \right).$$

We recognize that the vector $\frac{(\mathbf{E}\mathbf{y})_\ell}{w_\ell} \Phi_{*,\ell}$ is the ℓ th column of the matrix $\mathbf{K} := \Phi \text{diag}\{\mathbf{E}\mathbf{y} \odot \mathbf{w}^{-1}\}$. So, we have

$$\begin{aligned} \mathbf{1}^\top \sum_{\ell=1}^{n_t} w_\ell \mathbf{u}_\ell \odot \left(\frac{(\mathbf{E}\mathbf{y})_\ell}{w_\ell} \Phi_{*,\ell} \right) &= \mathbf{1}^\top \sum_{\ell=1}^{n_t} w_\ell (\mathbf{U} \odot \mathbf{K})_\ell \\ &= \mathbf{1}^\top (\mathbf{U} \odot \mathbf{M}\mathbf{M}^{-1}\mathbf{K}) \mathbf{w} \end{aligned}$$

$$= \langle\langle \mathbf{U}, \mathbf{M}^{-1} \mathbf{K} \rangle\rangle_{\mathbf{M}},$$

where in the last step we have used (54a). Hence, we yield the desired result, since for every $\mathbf{y} \in \mathbb{R}^{n_y}$,

$$\langle \mathbf{B}\mathbf{U}, \mathbf{y} \rangle_2 = \mathbf{1}^\top (\mathbf{U} \odot \Phi) \mathbf{E} \mathbf{y} = \langle\langle \mathbf{U}, \mathbf{M}^{-1} \mathbf{K} \rangle\rangle_{\mathbf{M}}.$$

□

We comment on the efficiency of applying \mathbf{B} and its adjoint to elements in their respective spaces. Given a path parameter ξ , we must form the matrix Φ . Since ϕ_i are compactly supported, Φ is sparse. We can build Φ with a geometric approach—only evaluating basis functions whose support contains the point \mathbf{r}_ℓ . Explicit construction and manipulation of the extraction matrix \mathbf{E} can be avoided with indexing.

The inverse problem. We are now ready to formulate the discretized inverse problem. The inversion parameter is given by the finite element coefficients $\mathbf{m} \in \mathbb{R}_{\mathbf{M}}^{n_x}$ corresponding to the approximation m_h of $m \in \mathcal{M}$. We treat \mathbf{m} as a random variable and seek a posterior distribution through Bayesian inversion. A key component in this construction is the discretized forward operator $\mathbf{F} : \mathbb{R}_{\mathbf{M}}^{n_x} \rightarrow \mathbb{R}^{n_y}$, defined by

$$\mathbf{F}(\xi) := \mathbf{B}(\xi) \mathbf{S}. \quad (65)$$

Analogous to the infinite-dimensional setting, data are acquired according to $\mathbf{y} = \mathbf{F}(\xi) \mathbf{m} + \boldsymbol{\eta}$, where $\boldsymbol{\eta}$ is the same Gaussian noise as in (4). Under the assumption that \mathbf{m} and $\boldsymbol{\eta}$ are uncorrelated, $\mathbf{y} | \mathbf{m} \sim \mathcal{N}(\mathbf{F}\mathbf{m}, \sigma^2 \mathbf{I})$.

The prior law for \mathbf{m} is $\mu_{\text{pr}} = \mathcal{N}(\mathbf{m}_{\text{pr}}, \boldsymbol{\Gamma}_{\text{pr}})$, where $\boldsymbol{\Gamma}_{\text{pr}}$ is the finite-element discretization of the elliptic differential operator in (7). Combining the data likelihood with the prior, we apply Bayes theorem to obtain the posterior law $\mu_{\text{post}}^{\mathbf{y}, \xi} = \mathcal{N}(\mathbf{m}_{\text{MAP}}^{\mathbf{y}}, \boldsymbol{\Gamma}_{\text{post}})$, where

$$\boldsymbol{\Gamma}_{\text{post}}(\xi) = (\sigma^{-2}(\mathbf{F}^* \mathbf{F})(\xi) + \boldsymbol{\Gamma}_{\text{pr}}^{-1})^{-1} \quad \text{and} \quad \mathbf{m}_{\text{MAP}}^{\mathbf{y}}(\xi) = \boldsymbol{\Gamma}_{\text{post}}(\xi) (\sigma^{-2} \mathbf{F}^*(\xi) \mathbf{y} + \boldsymbol{\Gamma}_{\text{pr}}^{-1} \mathbf{m}_{\text{pr}}). \quad (66)$$

The discretized Hessian, which is derived from the variational characterization of the MAP point, is given by

$$\mathbf{H}(\xi) = \mathbf{H}_{\text{mis}}(\xi) + \boldsymbol{\Gamma}_{\text{pr}}^{-1}, \quad \text{where} \quad \mathbf{H}_{\text{mis}}(\xi) = \sigma^{-2}(\mathbf{F}^* \mathbf{F})(\xi) \quad (67)$$

is the data-misfit Hessian. Again, we have the important identity $\mathbf{H}(\xi) = \boldsymbol{\Gamma}_{\text{post}}^{-1}(\xi)$.

For a scalable numerical framework we must be able to apply $\boldsymbol{\Gamma}_{\text{post}}$ to vectors in $\mathbb{R}_{\mathbf{M}}^{n_x}$ efficiently. We follow the approach outlined in [9], where a low-rank spectral decomposition and the Sherman–Morrison–Woodbury formula are used to obtain an approximation $\boldsymbol{\Gamma}_{\text{post},r}$ to $\boldsymbol{\Gamma}_{\text{post}}$. For $\xi \in \mathbb{R}^N$, let $\{(\lambda_i(\xi), \mathbf{v}_i(\xi))\}_{i=1}^r$ be the r leading eigenpairs of the *prior-preconditioned the data misfit Hessian* $\boldsymbol{\Gamma}_{\text{pr}}^{1/2} \mathbf{H}_{\text{mis}}(\xi) \boldsymbol{\Gamma}_{\text{pr}}^{1/2}$. Then, the action of $\boldsymbol{\Gamma}_{\text{post},r}(\xi)$ on $\mathbf{m} \in \mathbb{R}_{\mathbf{M}}^{n_x}$ is defined by

$$\boldsymbol{\Gamma}_{\text{post},r}(\xi) \mathbf{m} := \boldsymbol{\Gamma}_{\text{pr}} \mathbf{m} - \sum_{i=1}^r \frac{\lambda_i(\xi)}{\lambda_i(\xi) + 1} \langle \mathbf{m}, \boldsymbol{\Gamma}_{\text{pr}}^{1/2} \mathbf{v}_i(\xi) \rangle_{\mathbf{M}} \boldsymbol{\Gamma}_{\text{pr}}^{1/2} \mathbf{v}_i(\xi). \quad (68)$$

5.3 The discretized path-OED problem

Here we discretize the c-optimality criterion and its gradient introduced in Section 3. We then specialize these results to the c-optimality criterion used in our numerical experiments, discussed in Subsection 3.4.

Recall the infinite-dimensional representation of the c-optimality criterion in (18). The corresponding discretized criterion is given by

$$\Psi(\xi) := \langle \boldsymbol{\Gamma}_{\text{post}}(\xi) \mathbf{c}, \mathbf{c} \rangle_{\mathbf{M}}, \quad (69)$$

where \mathbf{c} is a fixed vector in $\mathbb{R}_{\mathbf{M}}^{n_x}$. Also, for $j \in \{1, \dots, N\}$, we recall the formula for $\partial_j \Psi$ in (28). Replacing the present operators with their discrete analogues, we obtain the following derivative formula:

$$\partial_j \Psi = -2\sigma^{-2} \langle \mathbf{B} \mathbf{S} \boldsymbol{\Gamma}_{\text{post}} \mathbf{c}, (\partial_j \mathbf{B}) \mathbf{S} \boldsymbol{\Gamma}_{\text{post}} \mathbf{c} \rangle_2. \quad (70)$$

It is straightforward to show that for any $\mathbf{U} \in \mathbb{R}_{\mathbf{M}}^{n_x \times n_t}$, the action of $\partial_j \mathcal{B}$ on \mathbf{U} is such that

$$(\partial_j \mathbf{B}(\xi)) \mathbf{U} = \partial_j (\mathcal{E} \mathbf{U} \odot \mathcal{E} \boldsymbol{\Phi}(\xi))^\top \mathbf{1} = (\mathcal{E} \mathbf{U} \odot \mathcal{E} \partial_j \boldsymbol{\Phi}(\xi))^\top \mathbf{1}. \quad (71)$$

Furthermore, the j th partial of $\Phi : \mathbb{R}^N \rightarrow \mathbb{R}^{n_x \times n_t}$, defined in (59), is given by

$$(\partial_j \Phi(\xi))_{i\ell} = \partial_j \phi_i(\mathbf{r}_\ell(\xi)) = \nabla \phi_i(\mathbf{r}_\ell(\xi)) \cdot \partial_j \mathbf{r}_\ell(\xi), \quad (72)$$

where $i \in \{1, 2, \dots, n_x\}$ and $\ell \in \{1, 2, \dots, n_t\}$.

The specific criterion. We next consider the goal-functional Z in (31) which we use to form the specific c-optimality criterion in Subsection 3.4. For a fixed $\mathbf{V} \in \mathbb{R}_M^{n_x \times n_t}$, the discretized analogue of Z is

$$\mathbf{Z}(\mathbf{m}) := \langle \langle \mathbf{V}, \mathbf{S}\mathbf{m} \rangle \rangle_M = \langle \mathbf{S}^* \mathbf{V}, \mathbf{m} \rangle_M, \quad \mathbf{m} \in \mathbb{R}_M^{n_x}. \quad (73)$$

Hence, taking $\mathbf{c} = \mathbf{S}^* \mathbf{V}$ in (69), the specific discretized criterion and its derivative are

$$\Psi(\xi) = \langle \mathbf{T}_{\text{post}}(\xi) \mathbf{S}^* \mathbf{V}, \mathbf{S}^* \mathbf{V} \rangle_M, \quad (74a)$$

$$\partial_j \Psi = -2\sigma^{-2} \langle \mathbf{B}(\xi) \mathbf{S} \mathbf{T}_{\text{post}}(\xi) \mathbf{S}^* \mathbf{V}, (\partial_j \mathbf{B}(\xi)) \mathbf{S} \mathbf{T}_{\text{post}}(\xi) \mathbf{S}^* \mathbf{V} \rangle_2. \quad (74b)$$

The procedure for computing $\Psi(\xi)$ and $\nabla \Psi(\xi)$ are outlined in Algorithm 1.

Algorithm 1 Algorithm for computing Ψ in (74a) and $\nabla \Psi$ defined by (74b)

```

1: Input: design  $\xi \in \mathbb{R}^N$ 
2: Output:  $\Psi(\xi)$  and  $\nabla \Psi(\xi)$ 
3: Compute  $\mathbf{c} := \mathbf{S}^* \mathbf{V}$ 
4: Compute  $\tilde{\mathbf{c}} := \mathbf{T}_{\text{post},r} \mathbf{c}$  ▷ with  $\mathbf{T}_{\text{post},r}$  as in (68)
5: Compute  $\Psi(\xi) = \langle \tilde{\mathbf{c}}, \mathbf{c} \rangle_M$ 
6: Compute  $\tilde{\mathbf{V}} := \mathbf{S} \tilde{\mathbf{c}}$ 
7: Compute  $\mathbf{d} := \mathbf{B}(\xi) \tilde{\mathbf{V}}$ 
8: for  $j = 1$  to  $N$  do
9:   Compute  $\mathbf{v}_j := (\partial_j \mathbf{B}(\xi)) \tilde{\mathbf{V}}$  ▷ with  $\partial_j \mathbf{B}(\xi)$  as in (71)
10:  Set  $\partial_j \Psi(\xi) = -2\sigma^{-2} \langle \mathbf{d}, \mathbf{v}_j \rangle_2$ 
11: end for
12: return  $\Psi(\xi)$  and  $\nabla \Psi(\xi)$ 

```

5.4 Computational considerations

We design the discretized path-OED framework so that standard gradient-based optimization algorithms can be used to minimize Ψ . The computational cost of this process depends primarily on two components: evaluation of the sensor parameterization $\mathbf{r}(t; \xi)$ and repeated application of operators arising from the inverse problem. In practice, the dominant cost is associated with applying the discretized solution operator and its adjoint, which appear multiple times in Algorithm 1, most notably through the low-rank approximation to the posterior covariance operator. While applying the discretized prior covariance operator $\mathbf{\Gamma}_{\text{pr}}$ also requires PDE solves, this cost is typically negligible when compared to applications of \mathbf{S} and \mathbf{S}^* . Hence, in what follows, we quantify cost in terms of *PDE solves*, meaning applications of \mathbf{S} or \mathbf{S}^* .

Forming the observation operator. As outlined in Subsection 5.2, for a given $\xi \in \mathbb{R}^N$, applying $\mathbf{B}(\xi)$ and its adjoint $\mathbf{B}^*(\xi)$ requires evaluating the path $\mathbf{r}(t; \xi)$ over the temporal discretization $\{t_\ell\}_{\ell=1}^{n_t}$. The expensiveness of this computation depends entirely upon the selected parameterization. For the path types presented in this work—Fourier and Bézier—this is very cheap. Specifically, computing the Fourier path in (36) requires N_f evaluations of cosine and sine over the set $\{t_\ell\}_{\ell=1}^{n_t}$. For the Bézier path (35), we can utilize de Casteljau’s algorithm [6]. This can be efficiently implemented with software like the Python package `bezier` [20], used in our implementation.

Applying the posterior covariance operator. In Section 6 we use the low-rank approximation $\mathbf{\Gamma}_{\text{post},r}$ in (68) to the discretized posterior covariance operator $\mathbf{\Gamma}_{\text{post}}$. As discussed in Subsection 5.2, applying $\mathbf{\Gamma}_{\text{post},r}$ to vectors in $\mathbb{R}_M^{n_x}$ involves solving an eigenvalue problem: we require the leading eigenvalues and eigenvectors

of the *prior-preconditioned data misfit Hessian* $\sigma^{-2}\mathbf{\Gamma}_{\text{pr}}^{1/2}(\mathbf{F}^*\mathbf{F})(\boldsymbol{\xi})\mathbf{\Gamma}_{\text{pr}}^{1/2}$. Since $\mathbf{B}(\boldsymbol{\xi})$ is a mapping from $\mathbb{R}_{\mathbf{M}}^{n_x \times n_t}$ to \mathbb{R}^{n_y} and $\mathbf{F}(\boldsymbol{\xi}) = \mathbf{B}(\boldsymbol{\xi})\mathbf{S}$, the rank of $(\mathbf{F}^*\mathbf{F})(\boldsymbol{\xi})$ is at most n_y . Thus, we choose the target rank r such that $r \leq n_y$, and computing the r leading eigenpairs requires $k \geq r$ iterations of the Lanczos method. Since each iteration involves applying both \mathbf{S} and \mathbf{S}^* , the resulting computation requires $2k$ PDE solves.

Computing the criterion and gradient. Referring to Algorithm 1, we observe that the computations required to evaluate Ψ are reused when forming $\nabla\Psi$. Hence, we can accumulate the total number of PDE solves required for both computations. Applying \mathbf{S}^* to \mathbf{V} in Line 3 of the Algorithm 1 requires a single PDE solve and, as noted above, computing $\mathbf{\Gamma}_{\text{post},r}(\boldsymbol{\xi})(\mathbf{S}^*\mathbf{V})$ in Line 4 results in $2k$ additional solves. Thus, evaluating Ψ requires $2k+1$ PDE solves. To compute the gradient, we apply \mathbf{S} once more in Line 6, bringing the total number of PDE solves in Algorithm 1 to $2k+2$, where $k \geq r$ denotes the number of Lanczos iterations required to compute the rank- r approximation $\mathbf{\Gamma}_{\text{post},r}$.

A PDE-free approach. We remark that PDE solves can be entirely avoided in Algorithm 1 by replacing the discretized solution operator with a surrogate. However, this is not achieved by simply substituting \mathbf{S} with a precomputed matrix, since its codomain $\mathbb{R}_{\mathbf{M}}^{n_x \times n_t}$ is a space of matrices equipped with the inner product shown in (53). Consequently, surrogates must respect the underlying Hilbert space structure; for example, neural operators or tensor decompositions constructed to preserve these inner products can be considered.

6 Computational results

We now demonstrate our framework on an example problem. Two variants are considered: one with Bézier paths and the other Fourier paths. The aim is not to compare their performance, which depends on the specific problem, but to illustrate that our path-OED formulation is stable under a change in path type.

6.1 A motivating problem

Consider the convection-diffusion equation

$$\begin{aligned} u_t - \alpha\Delta u + \mathbf{F} \cdot \nabla u &= m(\mathbf{x})a(t) && \text{in } \Omega \times T, \\ u &= 0, && \text{on } E_0 \times T, \\ \nabla u \cdot \mathbf{n} &= 0, && \text{on } E_n \times T, \\ u(\mathbf{x}, 0) &= u_0(\mathbf{x}, t), && \text{in } \Omega. \end{aligned} \tag{75}$$

This equation models the diffusive transport of a contaminant concentration over time. We let the domain Ω be $(0, 1)^2$ with boundary $\partial\Omega = E_0 \cup E_n$, where $E_0 \cap E_n = \emptyset$. The diffusion constant α is set to $\alpha = 0.15$. We specify the velocity field \mathbf{F} in the numerical experiments in Sections 6.2 and 6.3. For all numerical experiments we assume $u_0 \equiv 0$.

The inverse problem seeks to estimate m in (75) using measurements of u collected by a moving sensor. Here, the solution operator \mathcal{S} maps the inversion parameter m —the spatial component of the source term—to the solution u of (75). Applying the adjoint of \mathcal{S} to a vector requires an adjoint PDE solve. This is described in Appendix E, in the discretized setting. We use a Gaussian prior as discussed in Section 2. Specifically, we use $(a_1, a_2) = (5.5 \times 10^{-1}, 6 \times 10^{-3})$ in (7). As mentioned in Section 2, we assumed that observation errors are constant and uncorrelated. Subsequently, we take the noise variance in the following experiments to be $\sigma^2 = 10^{-3}$, resulting in approximately 1% noise.

The path-OED problem consists of minimizing the c-optimality criterion Ψ discussed in Subsection 3.4. Recall that Ψ characterizes the variance of a goal-functional $Z = \langle\langle v, u(m) \rangle\rangle$ where $u(m) = \mathcal{S}m$ is the solution to (75) and $v \in \mathcal{U}$. We choose v to be an indicator function for a spatiotemporal region $\Omega_v \times T_v$. Here, $\Omega_v \subset \Omega$ is open and $T_v \subset T$ is an interval such that $t_v > t$ for all $(t_v, t) \in T_v \times T_y$. Subsequently, v is defined by

$$v(\mathbf{x}, t) := \begin{cases} 1, & (\mathbf{x}, t) \in \Omega_v \times T_v, \\ 0, & (\mathbf{x}, t) \notin \Omega_v \times T_v, \end{cases} \tag{76}$$

so our example goal-functional is then

$$Z(m) = \langle\langle v, u(m) \rangle\rangle = \int_{T_v} \int_{\Omega_v} v(\mathbf{x}, t) u(\mathbf{x}, t) d\mathbf{x} dt. \quad (77)$$

Hence, Z quantifies the concentration of the solution u over some spatial region Ω_v and time interval T_v .

For the following analysis, we note that $Z(m)$ is a univariate random variable. Specifically, in the case that $\mu = \mathcal{N}(\bar{m}, \mathcal{C})$ is a Gaussian probability law, Z is Gaussian with expectation and variance given by

$$\mathbb{E}_\mu\{Z(m)\} = \langle \mathcal{S}^* v, \bar{m} \rangle \quad \text{and} \quad \mathbb{V}_\mu\{Z(m)\} = \langle \mathcal{C} \mathcal{S}^* v, \mathcal{S}^* v \rangle. \quad (78)$$

Hence, we can obtain an analytic formula for the probability density function (PDF) associated with $Z(m)$. When $\mu = \mu_{\text{post}}^{\mathbf{y}, \boldsymbol{\xi}}$, this PDF is termed the *posterior goal-density* and is used to assess how effectively an optimal design infers the synthetic true goal-value.

We must discretize v to form the discrete optimality criterion Ψ in (74). For the times $\{t_\ell\}_{\ell=1}^{n_t}$ in the discretization of T , define the indicator vector $\mathbf{v}_t \in \mathbb{R}^{n_t}$ by

$$(\mathbf{v}_t)_\ell := \begin{cases} 1, & t_\ell \in T_v, \\ 0, & t_\ell \notin T_v. \end{cases} \quad (79)$$

Similarly, let $\mathbf{v}_x \in \mathbb{R}_M^{n_x}$ be the finite element coefficients for an indicator function on Ω_v . Then, the snapshot matrix corresponding to the discretization of v is $\mathbf{v}_x \mathbf{v}_t^\top \in \mathbb{R}_M^{n_x \times n_t}$ and the discretized criterion is

$$\Psi(\boldsymbol{\xi}) = \langle \mathbf{\Gamma}_{\text{post}}(\boldsymbol{\xi}) \mathbf{S}^*(\mathbf{v}_x \mathbf{v}_t^\top), \mathbf{S}^*(\mathbf{v}_x \mathbf{v}_t^\top) \rangle_M. \quad (80)$$

Lastly, we discuss the discretization level and techniques used to solve the path-OED problem. For all experiments, we use $n_x = 35^2$ uniformly spaced spatial grid points and $n_t = 400$ time steps. Finite element discretization is performed using the FEniCS software package [3]. As discussed in Remark 1, the optimality criterion is nonconvex with potentially multiple local minima. Thus, we minimize Ψ with the limited-memory Broyden–Fletcher–Goldfarb–Shanno (L-BFGS) algorithm [11], as implemented in SciPy [45]. To address sensitivity of the results with respect to the choice of initial iterate, we perform multiple optimization runs with 10 initial iterates drawn via Latin hypercube sampling [30], using relaxed convergence tolerances. The best candidate is then used to initialize a final run with stricter tolerances.

6.2 An experiment with Bézier paths

Here we demonstrate our framework with Bézier paths. After discussing the experimental configuration, we solve the inverse problem and visualize some posterior samples. Next, we solve two variants of the path-OED problem: one where the initial and terminal positions of the paths do not coincide, and one where they do coincide (resulting in closed Bézier paths). Lastly, we perform a study with an obscured region, representing an area where data are not useful.

Problem setup. For boundary conditions in (75), we take E_0 to be the union of the *left* and *top* of Ω , and E_n as the union of the *right* and *bottom* sides. The global time interval is set to $T = [0, 1]$ and the inversion interval is $T_y = [0.2, 0.4]$. The sensor makes measurements at every other time step in the discretization of T_y , resulting in 40 measurement times. The velocity field and amplitude function in (75) are set to

$$\mathbf{F}(\mathbf{x}) = \begin{bmatrix} 1/\sqrt{2} \\ -1/\sqrt{2} \end{bmatrix} \quad \text{and} \quad a(t) = -\frac{1}{4} \cos(4\pi t) + \frac{3}{4}.$$

We depict the velocity and amplitude in Figure 3. With this model setup, the concentration alternates between amplification and damping, while being transported in the direction of outflow.

Lastly, we specify the subregions used to define the spatiotemporal indicator function v in (76). We select

$$\Omega_v = (0.5, 0.9) \times (0.1, 0.5) \quad \text{and} \quad T_v = [0.8, 1].$$

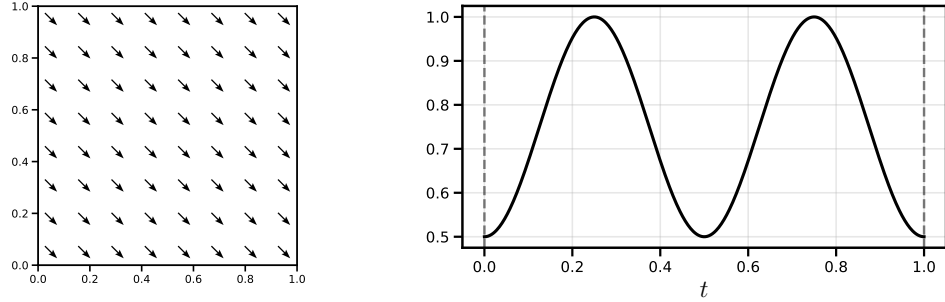


Fig. 3: The velocity field $\mathbf{F}(\mathbf{x})$ (left) and amplitude $a(t)$ (right) used for the Bézier experiment.

Solving the inverse problem. To demonstrate our framework we specify a ground truth inversion parameter m_{true} . This is decided to be a Gaussian-like function oriented in the upper-left quadrant of Ω . Applying the solution operator \mathcal{S} to m_{true} , we obtain the true solution $u_{\text{true}} := \mathcal{S}m_{\text{true}}$ to (75). We then collect data along a nominal Bézier path \mathbf{r}_b of degree 3 with control points $\{\mathbf{p}_0, \mathbf{p}_1, \mathbf{p}_2, \mathbf{p}_3\}$ specified by

$$\mathbf{p}_0 = \begin{bmatrix} 0.2 \\ 0.1 \end{bmatrix}, \mathbf{p}_1 = \begin{bmatrix} 0.2 \\ 2.5 \end{bmatrix}, \mathbf{p}_2 = \begin{bmatrix} 0.8 \\ -1.5 \end{bmatrix}, \mathbf{p}_3 = \begin{bmatrix} 0.8 \\ 0.9 \end{bmatrix}.$$

Figure 4 depicts u_{true} at the times $t \in \{0.1, 0.2, 0.3, 0.4\}$ together with the nominal Bézier path \mathbf{r}_b . The sensor begins its trajectory at $t = 0.2$ —its initial position indicated by the red dot in the second-from-left panel of Figure 4. The path is completed by $t = 0.4$, after which the simulation continues until $t = 1$.

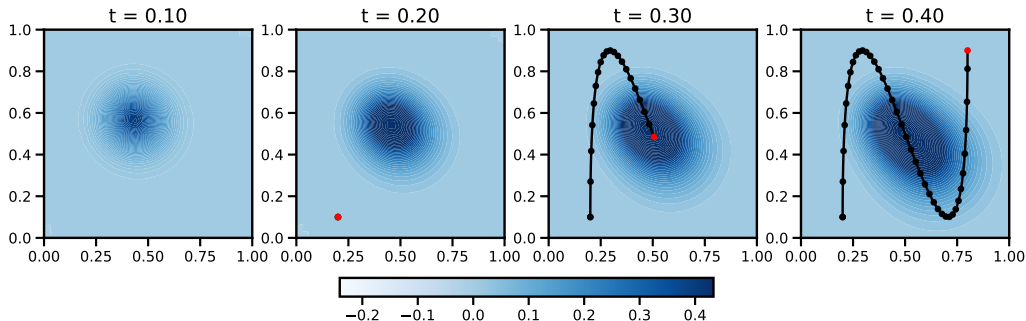


Fig. 4: Time-series of the solution $u_{\text{true}} = \mathcal{S}m_{\text{true}}$ and nominal Bézier path \mathbf{r}_b at four times. The red dot is the current position of the sensor and the black dots represent measurement locations.

We solve the inverse problem with 40 noisy measurements collected along the nominal path \mathbf{r}_b . Figure 5 depicts m_{true} (left) and three posterior samples. In the present experiment, the posterior samples capture the dominant features of the ground-truth parameter, even with limited data collected along a nominal path.

Solving the path-OED problem. Next we solve the path-OED problem with Bézier curves of degree $N_b = 5$. Two cases are considered: (i) the path starts at $(0.8, 0.2)$ and ends at $(0.2, 0.8)$; (ii) both the start and end positions are $(0.8, 0.2)$. Note that when the endpoints of a N_b -degree Bézier curve are fixed, the design vector ξ_b is composed by the interior control points. So in our case, $\xi_b \in \mathbb{R}^8$. To contain the curves in Ω , we require the control points to lie in Ω . As discussed in Subsection 4.2, this translates to a linear constraint on the design vector.

After solving the path-OED problem, we perform several experiments to assess the performance of the resulting design. First, we overlay the optimal paths on the corresponding *pointwise variance fields*; see [9]. This field quantifies posterior variance in the inversion parameter over the spatial domain. Next, we analyze the posterior goal-densities, computed using (78), and compare them to the true goal value $Z(m_{\text{true}})$. Finally,

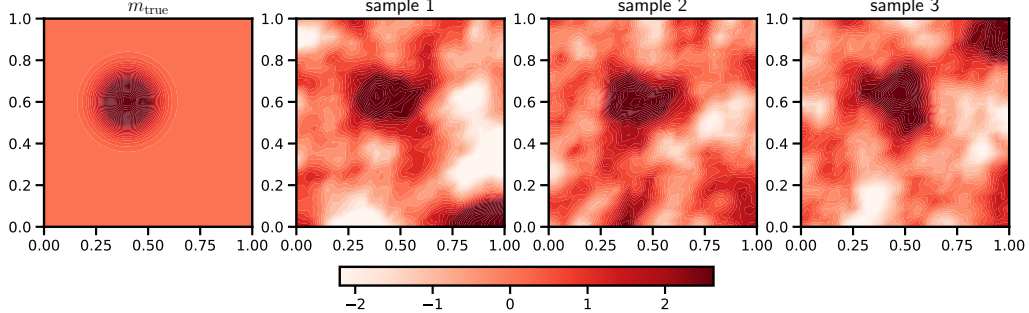


Fig. 5: The true parameter (left) and three posterior samples corresponding to the Bézier inverse problem.

to further assess optimality, we generate 1000 uniformly random designs $\xi_b \in \mathbb{R}^8$, evaluate the associated criterion values $\Psi(\xi_b)$, and compare their distribution to $Z(m_{\text{true}})$. The results are shown in Figure 6.

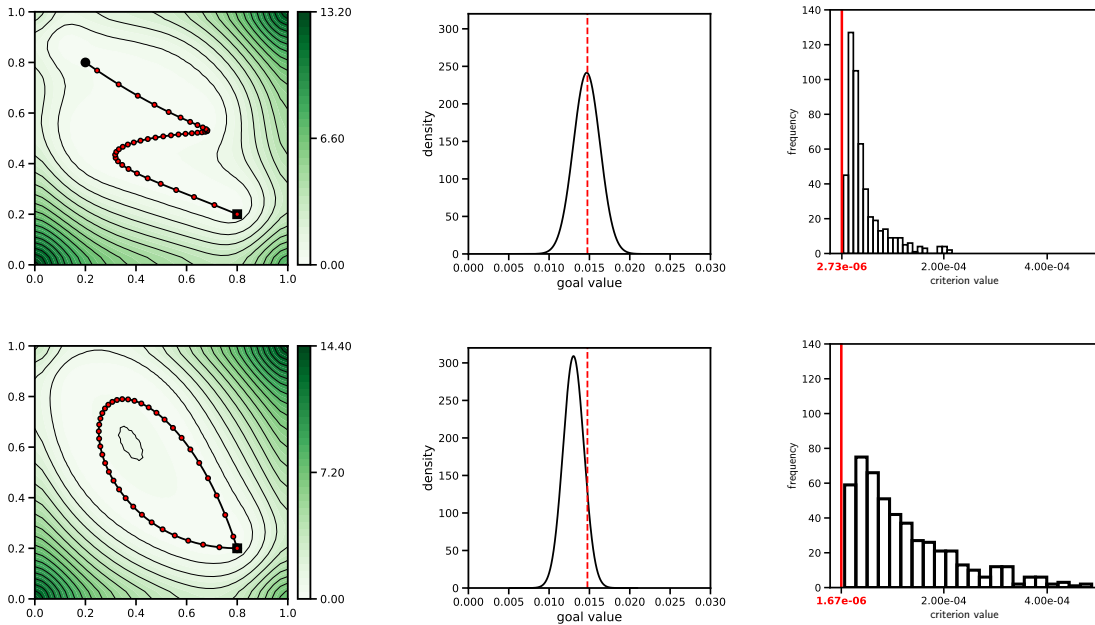


Fig. 6: Top: Results for a degree $N_b = 5$ Bézier curve where endpoints do not coincide. Bottom: Results for a degree $N_b = 5$ Bézier curve where endpoints do coincide. Left: Optimal path and pointwise parameter variance field. The square is the initial position of the path and circle is the terminal position. Middle: Posterior goal-density (true goal-value is the dotted vertical red line). Right: Optimal criterion value (vertical red line) and histogram of criterion values corresponding to uniformly random paths.

We first comment on the top row of Figure 6; the case where the initial and terminal positions of the optimal Bézier path are different. As seen in Figure 6 (top-left), the optimal path describes a Z-like trajectory. Where the sensor makes a sharp turn, a large amount of data is collected. This indicates that data in these regions are informative for goal inference. The posterior variance field plotted in the top-left of Figure 6 shows that the optimal design leads to preferential uncertainty reduction in the inversion parameter. That is, uncertainty is not reduced in every direction of \mathcal{M} , only in the important directions. The posterior goal-density in the top-middle of Figure 6 characterizes both the accuracy and certainty in goal inference. We note that the density is centered about the true goal-value and caution that the present behavior is influenced by the choice of the true parameter and data noise. Lastly, we consider the histogram of criterion

values in Figure 6 (top-right). We note that the optimal criterion value is lower when compared to values resulting from random designs. In fact, this difference is of order 10^2 . This implies that a suboptimal choice of the sensor path can lead to notably suboptimal reduction in the posterior uncertainty of Z .

We next repeat this study for the case where the initial and terminal positions coincide; see the bottom row of Figure 6. Here, we super-impose the computed optimal path over the posterior variance field in Figure 6 (bottom-left). The posterior goal-density in Figure 6 (bottom-middle) has a smaller variance than the corresponding result in the top panel, but is less-centered around the true goal-valued. Again, the relative position of the posterior goal-density to the true value should be carefully interpreted. It is worth noting, however, that the predicted posterior goal-density includes the ground-truth parameter in its high-probability region. Similar to the results for the non-coincident endpoints, the optimal criterion value is less than all the criterion values corresponding to randomly generated designs. This is shown in Figure 6 (bottom-right). Interestingly, the criterion values corresponding to the random designs span a wider range of values when compared to the top row results.

To further quantify the effectiveness of the optimal paths shown in Figure 6, we next examine the *coefficient of variation* for the goal functional. Given a probability law μ , the coefficient of variation, denoted by $CV(\mu)$, is defined as the ratio of the standard deviation of $Z(m)$ to the absolute value of its mean. So, $CV(\mu)$ is a unitless measure of uncertainty that we can calculate with the formulas in (78). Computing this value for the prior measure yields $C(\mu_{\text{pr}}) = 0.248$. For the posterior measure corresponding to the results in the top row of Figure 6, we have $CV(\mu_{\text{post}}^{y,\xi}) = 0.119$, and for the bottom row, $CV(\mu_{\text{post}}^{y,\xi}) = 0.109$. This results in a $\approx 52\%$ reduction the in CV when the initial and terminal endpoints of the path coincide, and when the endpoints do coincide, the reduction is $\approx 56\%$. Thus, the optimal design corresponding to the bottom row of Figure 6 yields slightly greater reduction in goal uncertainty than the other design.

A study with an obscured region and non-coincident endpoints. In this study we specify that the Bézier paths have initial position $(0.8, 0.2)$ and terminal position $(0.2, 0.8)$, and demonstrate our ability to solve the path-OED problem with an obscured region D ; see Subsection 4.2. Interpreting the model (75) as representing the concentration of some contaminant, D may describe a region that is obscured or where the sensor is unable to collect data effectively due to environmental factors. We take D to be a disk of radius $R_D = 0.16$ centered about $\mathbf{x}_D = (0.5, 0.5)$. The radial basis function p in (45), used to approximate an indicator function for D , is parameterized with $\beta = 0.01$.

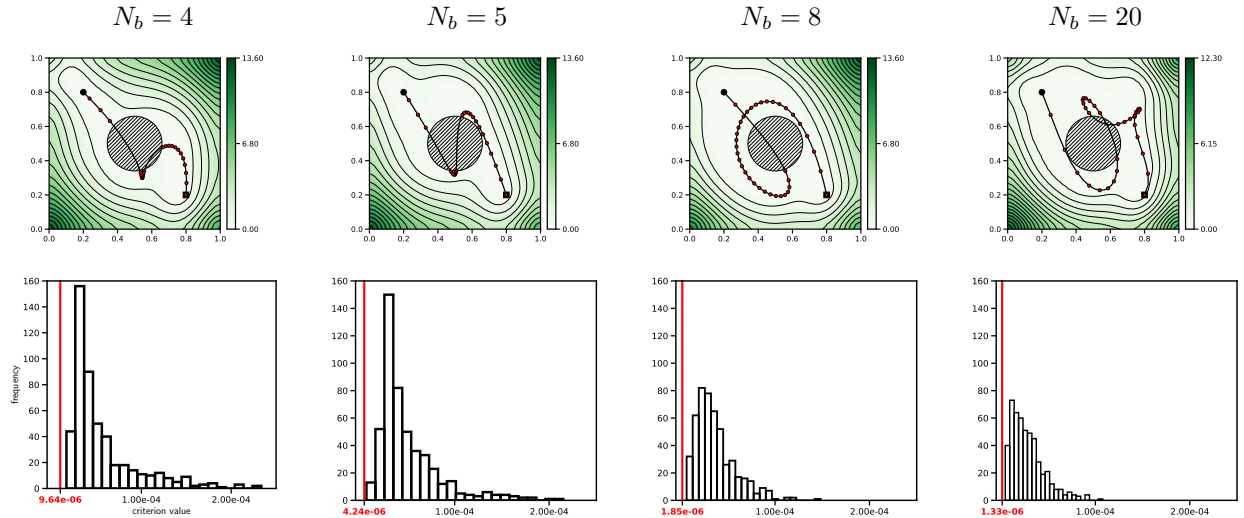


Fig. 7: Top: optimal paths for $N_b \in \{4, 5, 8, 20\}$ and corresponding posterior variance fields. The square is the initial position of the path and circle is the terminal position. The obscured region is represented by the shaded disk. Bottom: Histogram of criterion values for uniformly randomly generated designs. The optimal criterion value is the red vertical line.

In this experiment we illustrate how the degree of the Bézier curve impacts the results. To this end, we solve the path-OED problem with curves of degree $N_b \in \{4, 5, 8, 20\}$; see Figure 7. A key observation from the top row of Figure 7 is that the optimal paths enter the obscured region. This means that data is willingly sacrificed to explore more informative areas of Ω . This claim is exemplified with the $N_b = 8$ case. Here, the sensor completes most of a circumnavigation around the disk, then translates almost directly through the center to reach the terminal position. We also comment on the histograms in the bottom row of Figure 7. The optimal criterion value for the $N_b = 4$ case is 9.64×10^{-6} , and for $N_b = 20$, this value is 1.33×10^{-6} . Thus, increasing the design size by a factor of 5 results in less than an order 10 magnitude of improvement. This indicates that a relatively small degree number can be sufficient for informative designs. In all cases, the optimal criterion value is less than the criterion value corresponding to randomly generated designs. However, this discrepancy is greatest for a low degree number. This implies that path-OED is more effective when the number of control points is relatively small.

Now we revisit the earlier observation that optimal curves enter the obscured region. To provide further insight, we specify two intuitive paths that navigate opposite sides of D , instead of passing through. We compare the effectiveness of the optimal and selected paths by examining their respective posterior goal-densities. Figure 8 shows the optimal and specified paths (left) for $N_b = 5$ and corresponding posterior goal-densities (right). These results support our observation about quality over quantity of data. Although the selected paths navigate different sides of the obscured region, the widths of the corresponding posterior goal-densities are comparable. A sensor that travels along the optimal path loses many measurements by navigating through the obscured region, but is able to acquire more informative data. This observation is corroborated by the corresponding posterior goal-density, whose variance is substantially smaller when compared to the prescribed paths; see Figure 8 (right).

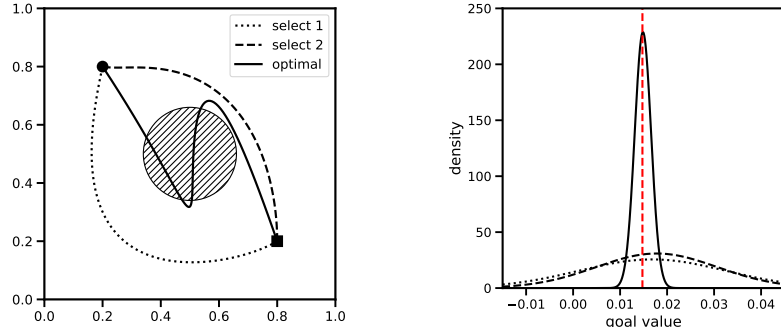


Fig. 8: Left: An optimal Bézier path and two selected paths of degree $N_b = 5$. Right: Posterior goal-densities corresponding to the optimal and selected paths. The red dotted line is the true goal-value.

A study with an obscured region and coincident endpoints. We repeat the previous experiment except we let the initial and terminal position of the sensor be $(0.8, 0.2)$, resulting in closed paths. Figure 9 shows optimal Bézier paths of degree $N_b \in \{4, 5, 8, 20\}$, posterior variance fields, and histograms of criterion values generated from evaluating the criterion at uniformly random designs. For $N_b \in \{4, 5, 8\}$, we see that the paths loop around the obscured region. When $N_b = 20$, this pattern is broken and the sensor performs a less intuitive maneuver. In this case, it is valuable to sacrifice data to obtain more informative measurements. Turning to the bottom row of Figure 9, we find that the degree $N_b \in \{4, 5\}$ optimal curves outperform the analogous results shown in Figure 7 in terms of criterion value. However, as we increase the size of the design, this pattern disappears and performance is comparable.

6.3 An experiment with Fourier paths

Here, we solve the path-OED problem with Fourier paths. In this case, we require the sensor's initial and terminal positions to coincide, forming a loop. However, we do not specify the starting location—this is

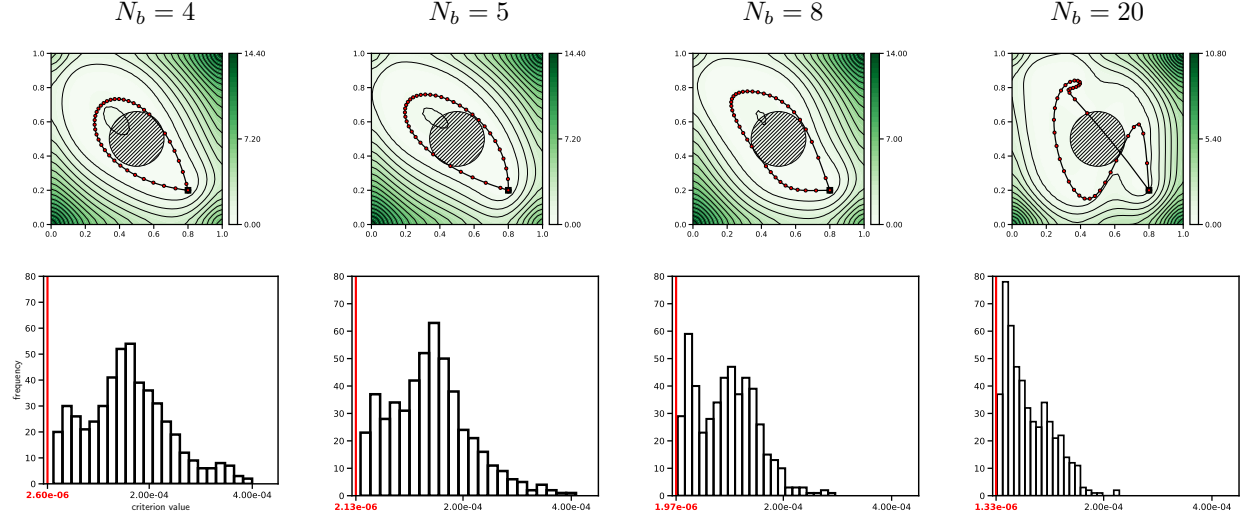


Fig. 9: Top: optimal paths for $N_b \in \{4, 5, 8, 20\}$ and corresponding posterior variance fields. The square is the initial/terminal position and the obscured region is the shaded disk. Bottom: Histogram of criterion values for uniformly randomly generated designs. The optimal criterion value is the red vertical line.

naturally determined by solving the path-OED problem. In what follows, after specifying the setup of the experiment, we solve the path-OED problem for various Fourier mode numbers N_f and discuss the results.

Problem setup. In the present experiment, the boundary conditions in (75) are selected such that $E_0 = \emptyset$ and $E_n = \partial\Omega$. That is, we consider only homogenous Neumann boundary conditions. The global time interval is $T = [0, 2]$ and the inversion interval is $T_y = [0.25, 1.0]$. The sensor makes a measurement at every third time instance in the discretization of T_y , resulting in 50 measurements. We let the velocity field and amplitude function in (75) to be

$$\mathbf{F}(\mathbf{x}) := \begin{bmatrix} 2(2x_2 - 1)(1 - (2x_1 - 1)^2) \\ -2(2x_1 - 1)(1 - (2x_2 - 1)^2) \end{bmatrix} \quad \text{and} \quad a(t) := \frac{1.05}{2} \left(1 - \frac{2}{\pi} \arctan(8t - 6) \right).$$

This defines a recirculating velocity field. As the concentration diffuses, it swirls about the point $(0.5, 0.5)$ while being damped by $a(t)$. We depict both the velocity field and amplitude function in Figure 10.

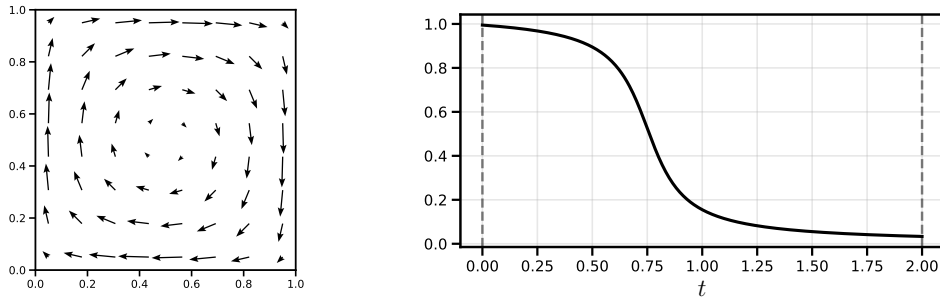


Fig. 10: The velocity field $\mathbf{F}(\mathbf{x})$ (left) and amplitude $a(t)$ (right) used for the Fourier experiment.

As for the spatiotemporal indicator function in (76) used to form Ψ , we define v with

$$\Omega_v = (0.2, 0.8)^2 \quad \text{and} \quad T_v = [1.5, 2].$$

Solving the path-OED problem. We consider Fourier paths with $N_f \in \{1, 3, 5, 10\}$ number of modes. For each N_f , we solve the path-OED problem by minimizing Ψ to yield the optimal design. The regularization

term $R(\xi_f; \gamma)$, presented in (42), is appended to Ψ to limit acceleration or sharp turns in the optimal paths. The choice of regularization parameter γ is depends upon the mode number. We select (N_f, γ) pairs as follows:

$$(N_f, \gamma) \in \{(1, 3 \times 10^{-7}), (3, 5 \times 10^{-9}), (5, 7 \times 10^{-10}), (10, 9 \times 10^{-11})\}.$$

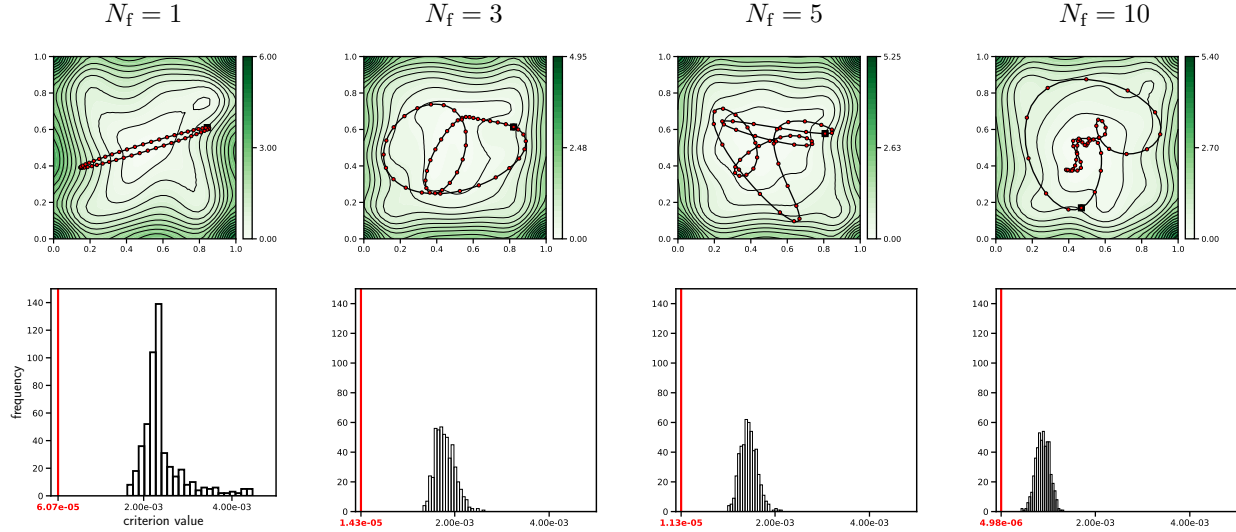


Fig. 11: Top: optimal paths for $N_f \in \{1, 3, 5, 10\}$ and corresponding posterior variance fields. The square is the initial/terminal position of the sensor. Bottom: Histogram of criterion values for uniformly randomly generated designs. The optimal criterion value is the red vertical line.

For each considered N_f , we study the optimal paths, posterior variance fields, and histograms of criterion values generated by evaluating $\Psi(\xi_f)$ for 1000 uniformly random ξ_f . These results are presented in Figure 11. As seen in the top row of the figure, the optimal paths become more complex as we increase N_f . For the $N_f = 1$ case, Fourier paths are ellipses. Hence, the top-left of Figure 11 shows the optimal ellipse. As with the Bézier experiments in Subsection 6.2, the optimal paths preferentially reduce uncertainty in regions of Ω that minimize variance in the goal-functional.

Now we examine the criterion value histograms on the bottom row of Figure 11. Optimal paths are consistently orders of magnitude better than randomly selected paths. This is indicated by the distance from the red vertical line (optimal criterion value) to the histograms in Figure 11. Increasing the number of the Fourier modes substantially reduces the optimal criterion value. This observation is supported by the factor 10 improvement on optimality achieved from $N_f = 5$ to $N_f = 10$. A significant observation is the large gap between the optimal criterion values and the values corresponding to randomly generated designs.

7 Conclusion

In this work we developed a mathematical and computational framework for optimal experimental design in infinite-dimensional Bayesian linear inverse problems with mobile sensors, which we termed *path-OED*. Our approach parameterizes sensor trajectories with any sufficiently regular family of curves. We define the observation operator by computing local averages of the PDE solution about measurement points on the sensor path. This results in a bounded linear observation operator, and enables us to deploy standard optimality criteria in the path-OED setting. We focused on the Bayesian c-optimality criterion and derived its derivatives. This was facilitated by a more general result which is useful beyond the path-OED setting: a formula for the derivative of a parameterized covariance-like operator. We also showed how practical constraints can be incorporated into the formulation. Proceeding from the function-space problem to a

finite-dimensional representation, we introduced a weighted time-space inner product and derived matrix-free actions of relevant operators and their adjoints. Numerical experiments showed that path-OED reduces prediction variance more effectively than random or user-prescribed paths.

The framework discussed in this article has several limitations and exposes directions for future research. For instance, it would be useful to extend path-OED to other criteria such as the A- and D-optimality criteria. The observation operator as formulated in the present work paves the way to formulating these criteria. However, formulas for their gradients and efficient computational methods must be derived. Also, the proposed approach assumes that the inversion model is linear. Subsequently, a path-OED framework for nonlinear infinite-dimensional Bayesian inverse problems is an open direction to research. In this case, the solution operator of the inverse problem is nonlinear. Known methods for addressing this nonlinearity include linearizing the solution operator, which would result in locally optimal solutions to the path-OED problem, constructing a Laplace approximation to the posterior, or relying on sampling based methods.

Other avenues to investigate include developments that make path-OED more practical to deploy in science and engineering applications. Our formulations are for a single sensor apparatus. Thus, we can consider adapting path-OED for an arbitrary number of mobile sensors. Our theoretical framework indicates how to carry out the infinite-dimensional formulation of this extension. However, considerable work is required to develop computational methods that enable solving path-OED problems with multiple sensors. We can also investigate how to incorporate constraints like battery life or obstacles into the path-OED problem. Other constraints arise depending on physical considerations related to the sensor apparatus and application.

Lastly, we remark on online extensions of path-OED or adaptations that incorporate sensor dynamics into the problem. Our approach is not online, meaning that the path-OED problem is solved before any data acquisition has occurred. In contrast, we can consider an online approach—utilizing ideas from sequential OED and data-assimilation. Advantages of such a formulation include the ability to incrementally update our prior with encountered data or the ability to respond to environmental hazards in real-time. Related to this concept, we can also adapt our path-OED approach to applications where dynamics governing the behavior of the sensor must be considered. For example, trajectories of the sensor can be considered as solutions to a dynamical system where the experimental design is a control input. This amounts to extending the formulations such as the ones in [42] to the present infinite-dimensional Bayesian formulations. This can be accomplished by noting that we can parameterize the control instead of the sensor trajectory directly.

Acknowledgments

This article has been authored by employees of National Technology & Engineering Solutions of Sandia, LLC under Contract No. DE-NA0003525 with the U.S. Department of Energy (DOE). The employees own all right, title and interest in and to the article and are solely responsible for its contents. SAND2026-16116O.

This material is also based upon work supported by the U.S. Department of Energy, Office of Science, Office of Advanced Scientific Computing Research Field Work Proposal Number 23-02526.

The work of Ahmed Attia was supported by the U.S. Department of Energy, Office of Science, Office of Advanced Scientific Computing Research, Scientific Discovery through Advanced Computing (SciDAC) Program through the FASTMath Institute under contract number DE-AC02-06CH11357 at Argonne National Laboratory.

References

- [1] Alen Alexanderian. Optimal experimental design for infinite-dimensional bayesian inverse problems governed by pdes: A review. *Inverse Problems*, 37(4):043001, 2021.
- [2] Alen Alexanderian, Philip J. Gloor, and Omar Ghattas. On Bayesian A- and D-Optimal Experimental Designs in Infinite Dimensions. *Bayesian Analysis*, 11(3), 2016.
- [3] Martin Alnæs, Jan Blechta, Johan Hake, August Johansson, Benjamin Kehlet, Anders Logg, Chris Richardson, Johannes Ring, Marie E Rognes, and Garth N Wells. The fenics project version 1.5. *Archive of numerical software*, 3(100), 2015.
- [4] Anthony C. Atkinson and Alexander N. Donev. *Optimum Experimental Designs*. Oxford, 1992.
- [5] Ahmed Attia, Alen Alexanderian, and Arvind K Saibaba. Goal-oriented optimal design of experiments for large-scale bayesian linear inverse problems. *Inverse Problems*, 34(9):095009, 2018.

- [6] Wolfgang Boehm and Andreas Müller. On de Casteljau's algorithm. *Computer Aided Geometric Design*, 16(7):587–605, 1999.
- [7] Haim Brézis. *Functional analysis, Sobolev spaces and partial differential equations*, volume 2. Springer, 2011.
- [8] M. D. Buhmann. Radial basis functions. *Acta Numerica*, 9:1–38, 2000.
- [9] Tan Bui-Thanh, Omar Ghattas, James Martin, and Georg Stadler. A computational framework for infinite-dimensional Bayesian inverse problems. Part I: The linearized case, with application to global seismic inversion. *SIAM Journal on Scientific Computing*, 35(6):A2494–A2523, 2013.
- [10] T Butler, John D Jakeman, and Tim Wildey. Optimal experimental design for prediction based on push-forward probability measures. *Journal of Computational Physics*, 416:109518, 2020.
- [11] Richard H Byrd, Peihuang Lu, Jorge Nocedal, and Ciyou Zhu. A limited memory algorithm for bound constrained optimization. *SIAM Journal on scientific computing*, 16(5):1190–1208, 1995.
- [12] Kathryn Chaloner and Isabella Verdinelli. Bayesian experimental design: A review. *Statistical Science*, 10(3):273–304, 1995.
- [13] Howie Choset, Kevin M Lynch, Seth Hutchinson, George A Kantor, and Wolfram Burgard. *Principles of robot motion: theory, algorithms, and implementations*. MIT press, 2005.
- [14] Masoumeh Dashti and Andrew M. Stuart. The Bayesian approach to inverse problems. In Roger Ghanem, David Higdon, and Houman Owhadi, editors, *Handbook of Uncertainty Quantification*, pages 311–428. Springer, 2017.
- [15] Matthew Dunbabin and Lino Marques. Robots for environmental monitoring: Significant advancements and applications. *IEEE Robotics & Automation Magazine*, 19(1):24–39, 2012.
- [16] Rida T. Farouki. The bernstein polynomial basis: A centennial retrospective. *Computer Aided Geometric Design*, 29(6):379–419, 2012.
- [17] A.R. Forrest. Interactive interpolation and approximation by bézier polynomials. *Computer-Aided Design*, 22(9):527–537, 1990.
- [18] Alessandro Gasparetto, Paolo Boscaroli, Albano Lanzutti, and Renato Vidoni. Path planning and trajectory planning algorithms: A general overview. *Motion and operation planning of robotic systems: Background and practical approaches*, pages 3–27, 2015.
- [19] Peter E Hart, Nils J Nilsson, and Bertram Raphael. A formal basis for the heuristic determination of minimum cost paths. *IEEE Transactions on Systems Science and Cybernetics*, 4(2):100–107, 1968.
- [20] Danny Hermes. Helper for bézier curves, triangles, and higher order objects. *The Journal of Open Source Software*, 2(16):267, Aug 2017.
- [21] Roger A Horn and Charles R Johnson. *Matrix analysis*. Cambridge University Press, 2012.
- [22] Xun Huan, Jayanth Jagalur, and Youssef Marzouk. Optimal experimental design: Formulations and computations. *Acta Numerica*, 33:715–840, 2024.
- [23] Karthik Karur, Nitin Sharma, Chinmay Dharmatti, and Joshua E. Siegel. A survey of path planning algorithms for mobile robots. *Vehicles*, 3(3):448–468, 2021.
- [24] Gregor Klančar, Marija Seder, Sašo Blažič, Igor Škrjanc, and Ivan Petrović. Drivable path planning using hybrid search algorithm based on e* and bernstein–bézier motion primitives. *IEEE Transactions on Systems, Man, and Cybernetics: Systems*, 51(8):4868–4882, 2019.
- [25] Tibor Kmet and Maria Kmetova. Bézier curve parametrisation and echo state network methods for solving optimal control problems of sir model. *Biosystems*, 186:104029, 2019. Selected papers from the International Conference on the Theory and Practice of Natural Computing 2017.
- [26] Jean-Claude Latombe. *Robot motion planning*, volume 124. Springer Science & Business Media, 2012.
- [27] Steven M LaValle. *Planning algorithms*. Cambridge University Press, 2006.
- [28] Steven M LaValle and James J Kuffner. Rapidly-exploring random trees: Progress and prospects: Steven m. lavalle, iowa state university, a. james j. kuffner, jr., university of tokyo, tokyo, japan. *Algorithmic and computational robotics*, pages 303–307, 2001.
- [29] Suwon Lee and Youdan Kim. Optimal output trajectory shaping using bézier curves. *Journal of Guidance, Control, and Dynamics*, 44(5):1027–1035, 2021.
- [30] Michael D McKay, Richard J Beckman, and William J Conover. A comparison of three methods for selecting values of input variables in the analysis of output from a computer code. *Technometrics*, 42(1):55–61, 2000.

- [31] Jiazhong Mei, Steven L. Brunton, and J. Nathan Kutz. Mobile sensor path planning for kalman filter spatiotemporal estimation. *Sensors*, 24(12), 2024.
- [32] J Nicholas Neuberger, Alen Alexanderian, and Bart van Bloemen Waanders. Goal oriented optimal design of infinite-dimensional bayesian inverse problems using quadratic approximations. *Journal of Scientific Computing*, 105(2):55, 2025.
- [33] Friedrich Pukelsheim. *Optimal Design of Experiments*. John Wiley & Sons, New-York, 1993.
- [34] Ewaryst Rafajłowicz. Optimum choice of moving sensor trajectories for distributed-parameter system identification. *International Journal of Control*, 43(5):1441–1451, 1986.
- [35] B. Naga Raju. Path planning based on Bézier curve for autonomous ground vehicles. *Journal of Science & Technology*, 7(10):112–115, Dec 2022.
- [36] Michael Reed and Barry Simon. *Methods of modern mathematical physics: Functional analysis*, volume 1. Gulf Professional Publishing, 1980.
- [37] Rastislav Róka. *Advanced Path Planning for Mobile Entities*. BoD–Books on Demand, 2018.
- [38] Ramanjeet Singh, Jing Ren, and Xianke Lin. A review of deep reinforcement learning algorithms for mobile robot path planning. *Vehicles*, 5(4):1423–1451, 2023.
- [39] Andrew M. Stuart. Inverse problems: A Bayesian perspective. *Acta Numerica*, 19:451–559, 2010.
- [40] Tingting Su, Long Cheng, Yunkuan Wang, Xu Liang, Jun Zheng, and Haojian Zhang. Time-optimal trajectory planning for delta robot based on quintic pythagorean-hodograph curves. *IEEE Access*, 6:28530–28539, 2018.
- [41] Christophe Tricaud and YangQuan Chen. *Optimal mobile sensing and actuation policies in cyber-physical systems*. Springer Science & Business Media, 2011.
- [42] Christophe Tricaud, Maciej Patan, Dariusz Uciński, and Yang Quan Chen. D-optimal trajectory design of heterogeneous mobile sensors for parameter estimation of distributed systems. In *2008 American Control Conference*, pages 663–668. IEEE, 2008.
- [43] Abera Tullu, Bedada Endale, Assefinew Wondosen, and Ho-Yon Hwang. Machine learning approach to real-time 3d path planning for autonomous navigation of unmanned aerial vehicle. *Applied Sciences*, 11(10):4706, 2021.
- [44] Dariusz Uciński. *Optimal measurement methods for distributed parameter system identification*. CRC Press, Boca Raton, 2005.
- [45] Pauli Virtanen, Ralf Gommers, Travis E. Oliphant, Matt Haberland, Tyler Reddy, David Cournapeau, Evgeni Burovski, Pearu Peterson, Warren Weckesser, Jonathan Bright, Stéfan J. van der Walt, Matthew Brett, Joshua Wilson, K. Jarrod Millman, Nikolay Mayorov, Andrew R. J. Nelson, Eric Jones, Robert Kern, Eric Larson, C J Carey, İlhan Polat, Yu Feng, Eric W. Moore, Jake VanderPlas, Denis Laxalde, Josef Perktold, Robert Cimrman, Ian Henriksen, E. A. Quintero, Charles R. Harris, Anne M. Archibald, Antônio H. Ribeiro, Fabian Pedregosa, Paul van Mulbregt, and SciPy 1.0 Contributors. SciPy 1.0: Fundamental Algorithms for Scientific Computing in Python. *Nature Methods*, 17:261–272, 2020.

Appendix A Proof of Theorem 1

The mollifiers defined in (13) are functions of time, space, and the path parameter ξ . We tend to suppress these dependencies for convenience, simply writing τ_k and δ_r .

Proof In the case that u is continuous, the integral $\langle\langle \tau_k \delta_r, u \rangle\rangle$ approximates $u(r_k, \tau_k)$. Of course, this interpretation is lost when u is only L^2 , as u may not be pointwise defined. To show Item 1 of Theorem 1, we refer the reader to Theorem 4.22 in [7]. This result states that we can approximate members of L^2 arbitrarily close (in the L^2 sense) via a sequence of convolutions with mollifier functions. When u is continuous, this becomes pointwise convergence.

Now, fix $\xi \in \mathbb{R}^N$ and consider the operator $\mathcal{B}(\xi)$. Linearity of \mathcal{B} is a direct consequence of the $\langle\langle \cdot, \cdot \rangle\rangle$ inner-product, defined in (6). As for boundedness, the Cauchy-Schwarz inequality provides that

$$\|\mathcal{B}u\|_2^2 = \sum_{k=1}^{n_y} \langle\langle \tau_k \delta_r, u \rangle\rangle^2 \leq \|u\|_{\mathcal{U}}^2 \sum_{k=1}^{n_y} \|\tau_k \delta_r\|_{\mathcal{U}}^2.$$

The mollifiers are strictly positive and bounded above. Furthermore, $\Omega \times T \subset \mathbb{R}^2 \times \mathbb{R}$ is a bounded set. Hence, $\|\tau_k \delta_r\|_{\mathcal{U}}^2 < \infty$, for any $k \in \{1, 2, \dots, n_y\}$, implying that \mathcal{B} is a bounded in \mathcal{U} .

Now we show that $\mathcal{B}(\cdot)$ is continuous in the path variable. For the following argument, note that $\|\tau_k\|_{L^\infty(T)}$ is finite and constant in k . Subsequently, define $\tau_\infty := \|\tau_k\|_{L^\infty(T)}$ and fix $\xi \in \mathbb{R}^N$. Then, for a sequence $\{\xi_n\}_{n=1}^\infty$ such that $\lim_{n \rightarrow \infty} \xi_n = \xi$ and any $u \in \mathcal{U}$, the Cauchy-Schwarz inequality provides that

$$\begin{aligned} \|\mathcal{B}(\xi_n) - \mathcal{B}(\xi)u\|_2^2 &= \sum_{k=1}^{n_y} \langle\langle \tau_k(\delta_r(\xi_n) - \delta_r(\xi)), u \rangle\rangle^2 \\ &\leq \|u\|_{\mathcal{U}}^2 \sum_{k=1}^{n_y} \|\tau_k(\delta_r(\xi_n) - \delta_r(\xi))\|_{\mathcal{U}}^2 \\ &\leq n_y \tau_\infty^2 \|u\|_{\mathcal{U}}^2 \|\delta_r(\xi_n) - \delta_r(\xi)\|_{\mathcal{U}}^2. \end{aligned}$$

In the case that $u \neq 0$,

$$\frac{\|\mathcal{B}(\xi_n) - \mathcal{B}(\xi)u\|_2}{\|u\|_{\mathcal{U}}} \leq n_y^{1/2} \tau_\infty \|\delta_r(\xi_n) - \delta_r(\xi)\|_{\mathcal{U}}. \quad (\text{A1})$$

We rewrite this by taking the supremum over the left side, obtaining the operator norm of $\mathcal{B}(\xi_n) - \mathcal{B}(\xi)$. Specifically,

$$\|\mathcal{B}(\xi_n) - \mathcal{B}(\xi)\| \leq n_y^{1/2} \tau_\infty \|\delta_r(\xi_n) - \delta_r(\xi)\|_{\mathcal{U}}. \quad (\text{A2})$$

To conclude the argument we show that the right side of (A2) vanishes. The mollifier functions $\delta_r(\mathbf{x}, t; \xi)$ are bounded above for any ξ . Thus, there must be some $K > 0$ such that

$$|\delta_r(\xi_n) - \delta_r(\xi)| < K, \quad \text{for all } n \in \mathbb{N}.$$

For any $(\mathbf{x}, t) \in \Omega \times T$, the term $\delta_r(\mathbf{x}, t; \xi)$ is a composition of continuous mappings in ξ . Thus,

$$\lim_{n \rightarrow \infty} |\delta_r(\xi_n) - \delta_r(\xi)|^2 = 0.$$

Subsequently, the Dominated Convergence Theorem provides that

$$\lim_{n \rightarrow \infty} \|\delta_r(\xi_n) - \delta_r(\xi)\|_{\mathcal{U}}^2 = \int_T \int_{\Omega} \lim_{n \rightarrow \infty} |\delta_r(\xi_n) - \delta_r(\xi)|^2 dx dt = 0.$$

It follows that the right side of (A2) vanishes and $\mathcal{B}(\cdot)$ must be continuous since

$$\lim_{n \rightarrow \infty} \|\mathcal{B}(\xi_n) - \mathcal{B}(\xi)\| = 0, \quad \text{whenever } \lim_{n \rightarrow \infty} \xi_n = \xi.$$

Lastly, we derive the adjoint of the observation operator. We note that for any $u \in \mathcal{U}$ and $\mathbf{y} \in \mathbb{R}^{n_y}$, the adjoint operator \mathcal{B}^* satisfies $\langle \mathcal{B}u, \mathbf{y} \rangle_2 = \langle \langle u, \mathcal{B}^* \mathbf{y} \rangle \rangle$. Performing a straightforward calculation, we find that

$$\langle \mathcal{B}u, \mathbf{y} \rangle_2 = \sum_{k=1}^{n_y} (\mathcal{B}u)_k y_k = \sum_{k=1}^{n_y} \langle \langle u, \tau_k \delta_r \rangle \rangle y_k = \langle \langle u, \delta_r \sum_{k=1}^{n_y} \tau_k y_k \rangle \rangle.$$

The resulting expression reveals the action of \mathcal{B}^* on \mathbf{y} . □

Appendix B Proof of Theorem 2

Proof We obtain the desired result by proving that

$$\lim_{h \rightarrow 0} \frac{1}{h} (\mathcal{C}(\xi + h) - \mathcal{C}(\xi)) = - \lim_{h \rightarrow 0} \mathcal{C}(\xi) \dot{\mathcal{H}}_0(\xi) \mathcal{C}(\xi). \quad (\text{B3})$$

Our argument uses that $\mathcal{C} : \mathbb{R} \rightarrow \mathcal{L}_{\text{sym}}^{++}(\mathcal{M})$ is continuous. Hence, we prove this fact first. Recall that $\mathcal{H} = \mathcal{H}_0 + \mathcal{C}_0^{-1}$ and $\mathcal{I} = \mathcal{C}\mathcal{H}$. Thus, $\mathcal{H}(\xi + h) - \mathcal{H}(\xi) = \mathcal{H}_0(\xi + h) - \mathcal{H}_0(\xi)$ and, by submultiplicativity of the operator norm,

$$\begin{aligned} \|\mathcal{C}(\xi + h) - \mathcal{C}(\xi)\| &= \|\mathcal{C}(\xi + h)(\mathcal{H}(\xi) - \mathcal{H}(\xi + h))\mathcal{C}(\xi)\| \\ &\leq \|\mathcal{C}(\xi)\| \|\mathcal{C}(\xi + h)\| \|\mathcal{H}_0(\xi) - \mathcal{H}_0(\xi + h)\|. \end{aligned} \quad (\text{B4})$$

Since \mathcal{H}_0 is Frechét differentiable, it is continuous and we have that $\lim_{h \rightarrow 0} \frac{1}{h} \|\mathcal{H}_0(\xi) - \mathcal{H}_0(\xi + h)\| = 0$. Thus, the right side of (B4) vanishes whenever $\mathcal{C}(\xi + h)$ is bounded. We prove this fact next.

Recall that $\mathcal{C}_0 \in \mathcal{L}_{\text{sym}}^{++}(\mathcal{M})$ and is not necessarily surjective. Subsequently, $\mathcal{C}_0^{1/2}$ exists and is a member of $\mathcal{L}_{\text{sym}}^{++}(\mathcal{M})$. The inverse of this operator, denoted by $\mathcal{C}_0^{-1/2}$, is possibly unbounded, self-adjoint, strictly positive, and defined on the range of $\mathcal{C}_0^{1/2}$. Hence, we form the operator $\tilde{\mathcal{H}}_0 = \mathcal{C}_0^{1/2} \mathcal{H}_0 \mathcal{C}_0^{1/2}$ and perform the factorization

$$\mathcal{C}(\xi + h) = \mathcal{C}_0^{1/2} (\tilde{\mathcal{H}}_0(\xi + h) + \mathcal{I})^{-1} \mathcal{C}_0^{1/2}. \quad (\text{B5})$$

Now, using the self-adjointness of $\mathcal{C}_0^{1/2}$, we have that

$$\|\mathcal{C}(\xi + h)\| = \left\| \mathcal{C}_0^{1/2} (\tilde{\mathcal{H}}_0(\xi + h) + \mathcal{I})^{-1} \mathcal{C}_0^{1/2} \right\| \leq \|\mathcal{C}_0\| \left\| (\tilde{\mathcal{H}}_0(\xi + h) + \mathcal{I})^{-1} \right\|. \quad (\text{B6})$$

Since $\mathcal{C}_0^{1/2} \in \mathcal{L}_{\text{sym}}^{++}(\mathcal{M})$ and $\mathcal{H}_0(\xi + h) \in \mathcal{L}_{\text{sym}}^+(\mathcal{M})$, we have that $\tilde{\mathcal{H}}_0(\xi + h) \in \mathcal{L}_{\text{sym}}^+(\mathcal{M})$, for any $\xi, h \in \mathbb{R}$. Thus, the spectrum of $\tilde{\mathcal{H}}_0(\xi + h)$ is a subset of $[0, \|\tilde{\mathcal{H}}_0(\xi + h)\|]$. Subsequently, shifting $\tilde{\mathcal{H}}_0(\xi + h)$ by \mathcal{I} then inverting yields

$$\left\| (\tilde{\mathcal{H}}_0(\xi + h) + \mathcal{I})^{-1} \right\| \leq 1.$$

Substituting this bound into (B6), we have that $\|\mathcal{C}(\xi + h)\| \leq \|\mathcal{C}_0\|$ and (B4) implies

$$\|\mathcal{C}(\xi + h) - \mathcal{C}(\xi)\| \leq \|\mathcal{C}(\xi)\| \|\mathcal{C}_0\| \|\mathcal{H}_0(\xi) - \mathcal{H}_0(\xi + h)\|.$$

It follows that \mathcal{C} is continuous since $\lim_{h \rightarrow 0} \|\mathcal{C}(\xi + h) - \mathcal{C}(\xi)\| = 0$.

Now we derive the formula for the derivative of \mathcal{C} . Since \mathcal{H}_0 is differentiable, $\dot{\mathcal{H}}_0 = \dot{\mathcal{H}} = \lim_{h \rightarrow 0} \frac{1}{h} (\mathcal{H}(\xi + h) - \mathcal{H}(\xi))$. Using this fact, the identity $\mathcal{I} \equiv \mathcal{C}\mathcal{H}$, and continuity of \mathcal{C} , we have that

$$\begin{aligned} 0 &= \lim_{h \rightarrow 0} \frac{1}{h} (\mathcal{C}(\xi + h)\mathcal{H}(\xi + h) - \mathcal{C}(\xi)\mathcal{H}(\xi)) \\ &= \lim_{h \rightarrow 0} \frac{1}{h} (\mathcal{C}(\xi + h)\mathcal{H}(\xi + h) - \mathcal{C}(\xi + h)\mathcal{H}(\xi)) + \lim_{h \rightarrow 0} \frac{1}{h} (\mathcal{C}(\xi + h)\mathcal{H}(\xi) - \mathcal{C}(\xi)\mathcal{H}(\xi)) \\ &= \lim_{h \rightarrow 0} \frac{1}{h} \mathcal{C}(\xi + h) (\mathcal{H}(\xi + h) - \mathcal{H}(\xi)) + \lim_{h \rightarrow 0} \frac{1}{h} (\mathcal{C}(\xi + h) - \mathcal{C}(\xi)) \mathcal{H}(\xi) \\ &= \mathcal{C}(\xi) \dot{\mathcal{H}}_0(\xi) + \lim_{h \rightarrow 0} \frac{1}{h} (\mathcal{C}(\xi + h) - \mathcal{C}(\xi)) \mathcal{H}(\xi) \end{aligned}$$

By subtracting the first term in the resulting expression and multiplying by $\mathcal{H}^{-1}(\xi)$, we obtain

$$\lim_{h \rightarrow 0} \frac{1}{h} (\mathcal{C}(\xi + h) - \mathcal{C}(\xi)) = -\mathcal{C}(\xi) \dot{\mathcal{H}}_0(\xi) \mathcal{C}(\xi). \quad (\text{B7})$$

□

Appendix C Gradient of the filtered c-optimality criterion

In what follows, we derive a formula for the derivative of the c-optimality criterion for an inverse problem modified to incorporate an obscured region. We recall the *filtered Hessian* \mathcal{H}_D as presented in (48) and Ψ in (18). Since $\mathcal{H}_D^{-1} \equiv \mathcal{C}_{\text{post}}$, the filtered c-optimality criterion can be written as

$$\Psi(\boldsymbol{\xi}) = \langle \mathcal{H}_D^{-1}(\boldsymbol{\xi})c, m \rangle = \langle \mathcal{C}_{\text{post}}(\boldsymbol{\xi})c, m \rangle. \quad (\text{C8})$$

We then derive the derivatives of (C8). To simplify subsequent calculations, we suppress dependency on $\boldsymbol{\xi}$.

Let $j \in \{1, \dots, N\}$ and recall that Theorem 4 provides that

$$\partial_j \Psi = -\langle (\partial_j \mathcal{H}_D) \mathcal{C}_{\text{post}} c, \mathcal{C}_{\text{post}} c \rangle. \quad (\text{C9})$$

Thus, we must compute $\partial_j \mathcal{H}_D$ and manipulate the resulting expressions. By the definition of \mathcal{H}_D ,

$$\begin{aligned} \partial_j \mathcal{H}_D &= \sigma^{-2} \mathcal{S}^* \partial_j (\mathcal{B}^* (\mathbf{I} - \mathbf{P}) \mathcal{B}) \mathcal{S} \\ &= \sigma^{-2} \mathcal{S}^* \partial_j (\mathcal{B}^* \mathcal{B}) \mathcal{S} - \sigma^{-2} \mathcal{S}^* \partial_j (\mathcal{B}^* \mathbf{P} \mathcal{B}) \mathcal{S}. \end{aligned} \quad (\text{C10})$$

We computed the first term of (C10) in the proof of Theorem 4. Hence, we seek a formula for $\partial_j (\mathcal{B}^* \mathcal{B})$.

Let $u \in \mathcal{U}$. Then, the definition of \mathcal{B} and its adjoint \mathcal{B}^* imply that

$$(\mathcal{B}^* \mathbf{P} \mathcal{B}) u = \delta_{\mathbf{r}} \sum_{k=1}^d \tau_k p_k \langle \langle \tau_k \delta_{\mathbf{r}}, u \rangle \rangle.$$

The resulting expression reveals a tensor representation for $\mathcal{B}^* \mathbf{P} \mathcal{B}$. Specifically,

$$\mathcal{B}^* \mathbf{P} \mathcal{B} = \sum_{k=1}^{n_y} \tau_k \delta_{\mathbf{r}} p_k \otimes \tau_k \delta_{\mathbf{r}}. \quad (\text{C11})$$

Applying Lemma 3 to (C11), we have that

$$\partial_j (\mathcal{B}^* \mathbf{P} \mathcal{B}) = \sum_{k=1}^{n_y} \tau_k \delta_{\mathbf{r}} p_k \otimes \tau_k \partial_j \delta_{\mathbf{r}} + \tau_k \partial_j (\delta_{\mathbf{r}} p_k) \otimes \tau_k \delta_{\mathbf{r}}. \quad (\text{C12})$$

Both $\delta_{\mathbf{r}}$ and p_k are continuously differentiable in the path parameter ξ . So,

$$\partial_j (\delta_{\mathbf{r}} p_k) = \delta_{\mathbf{r}} (\nabla p_k \cdot \partial_j \mathbf{r}_k) + p_k \partial_j \delta_{\mathbf{r}}. \quad (\text{C13})$$

Combining (C12), (C13), and our computation for $\partial_j (\mathcal{B}^* \mathcal{B})$ in (27), we write (C10) as¹

$$\begin{aligned} \partial_j \mathcal{H}_D &= \sigma^{-2} \mathcal{S}^* \left(\sum_{k=1}^{n_y} (1 - p_k) (\tau_k \delta_{\mathbf{r}} p_k \otimes \tau_k \partial_j \delta_{\mathbf{r}} + \tau_k \partial_j (\delta_{\mathbf{r}} p_k) \otimes \tau_k \delta_{\mathbf{r}}) \right) \mathcal{S} \\ &\quad - \sigma^{-2} \mathcal{S}^* \left(\sum_{k=1}^{n_y} (\nabla p_k \cdot \partial_j \mathbf{r}_k) \tau_k \delta_{\mathbf{r}} \otimes \tau_k \delta_{\mathbf{r}} \right) \mathcal{S}. \end{aligned} \quad (\text{C14})$$

In the last step we substitute (C14) back into (C9) then perform a series of manipulations; since $\nabla p_k \cdot \partial_j \mathbf{r}_k$ and $1 - p_k$ are scalars, we can factor them out of $\langle\langle \cdot, \cdot \rangle\rangle$. Subsequently, we find that

$$\begin{aligned} \partial_j \Psi &= -2\sigma^{-2} \sum_{k=1}^{n_y} (1 - p_k) \langle\langle \tau_k \delta_{\mathbf{r}}, \mathcal{S} \mathcal{C}_{\text{post}} c \rangle\rangle \langle\langle \tau_k \partial_j \delta_{\mathbf{r}}, \mathcal{S} \mathcal{C}_{\text{post}} c \rangle\rangle \\ &\quad - \sigma^{-2} \sum_{k=1}^{n_y} (\nabla p_k \cdot \partial_j \mathbf{r}_k) \langle\langle \tau_k \delta_{\mathbf{r}}, \mathcal{S} \mathcal{C}_{\text{post}} c \rangle\rangle^2. \end{aligned}$$

A more compact expression can be acquired recognizing the identities in (30):

$$\partial_j \Psi = -2\sigma^{-2} \langle \mathcal{B} \mathcal{S} \mathcal{C}_{\text{post}} c, (\mathbf{I} - \mathbf{P})(\partial_j \mathcal{B}) \mathcal{S} \mathcal{C}_{\text{post}} c \rangle_2 - \sigma^{-2} \langle \mathcal{B} \mathcal{S} \mathcal{C}_{\text{post}} c, (\partial_j \mathbf{P}) \mathcal{B} \mathcal{S} \mathcal{C}_{\text{post}} c \rangle_2. \quad (\text{C15})$$

Appendix D Proof of Theorem 6

Proof First we express the Fourier path \mathbf{r}_f as an affine transformation on $\xi_f \in \mathbb{R}^{4N_f}$. To do this, we first define

$$C_j := \cos(\omega_j t) \quad \text{and} \quad S_j := \sin(\omega_j t), \quad \text{with} \quad \omega_j = \frac{2\pi j}{|T_y|}. \quad (\text{D16})$$

We then build an operator $\mathbf{T}_f : T_y \rightarrow \mathbb{R}^{2 \times 4N_f}$ with action on ξ_f defined by

$$\mathbf{T}_f(t) \xi_f := \sum_{j=1}^{N_f} \begin{bmatrix} a_j C_j(t) + b_j S_j(t) \\ c_j C_j(t) + d_j S_j(t) \end{bmatrix}. \quad (\text{D17})$$

It is easy to show that for any $t \in T_y$, the transformation \mathbf{T}_f is linear in ξ_f . Hence, \mathbf{r}_f in (36) becomes

$$\mathbf{r}_f(t; \xi) = \bar{\mathbf{x}} + \mathbf{T}_f(t) \xi_f, \quad (\text{D18})$$

implying that \mathbf{r}_f is an affine transformation. Subsequently, Remark 3 provides that for any $R_\Omega > 0$,

$$\|\mathbf{r}_f - \bar{\mathbf{x}}\|_2 \leq R_\Omega, \quad \text{whenever} \quad \|\xi\|_2 \leq \frac{R_\Omega}{\sup_{t \in T_y} \|\mathbf{T}_f(t)\|_2}.$$

¹Here we use that if $u, v, u' \in U$, then for all $v' \in U$, $((u' u) \otimes v)v' = u'(u\langle\langle v, v' \rangle\rangle) = u'((u \otimes v)v')$. Hence, $(u' u) \otimes v = u'(u \otimes v)$.

We are then left to prove that $\|\mathbf{T}_f(t)\|_2 = \sqrt{N_f}$, for all $t \in T_y$, yielding the desired result.

In what follows we fix $t \in T_y$ and suppress this variable in our calculations. For $\mathbf{x} \in \mathbb{R}^2$, observe that

$$\begin{aligned}\mathbf{x}^\top \mathbf{T}_f \boldsymbol{\xi}_f &= x_1 \sum_{j=1}^{N_f} (a_j C_j + b_j S_j) + x_2 \sum_{j=1}^{N_f} (c_j C_j + d_j S_j) \\ &= \boldsymbol{\xi}_f^\top [x_1 C_1 \ x_1 S_1 \ x_2 C_1 \ x_2 S_1 \ \dots \ x_1 C_{N_f} \ x_1 S_{N_f} \ x_2 C_{N_f} \ x_2 S_{N_f}]^\top.\end{aligned}$$

This reveals the action of \mathbf{T}_f^\top on $\boldsymbol{\xi}_f$. Specifically,

$$\mathbf{T}_f^\top \mathbf{x} = [x_1 C_1 \ x_1 S_1 \ x_2 C_1 \ x_2 S_1 \ \dots \ x_1 C_{N_f} \ x_1 S_{N_f} \ x_2 C_{N_f} \ x_2 S_{N_f}]^\top.$$

This provides us with the following formula for the action of $\mathbf{T}_f^\top \mathbf{T}_f$ on $\boldsymbol{\xi}_f$:

$$\begin{aligned}(\mathbf{T}_f^\top \mathbf{T}_f) \boldsymbol{\xi}_f &= \left[\left(C_1 \sum_{j=1}^{N_f} a_j C_j + b_j S_j \right), \left(S_1 \sum_{j=1}^{N_f} a_j C_j + b_j S_j \right), \left(C_1 \sum_{j=1}^{N_f} c_j C_j + d_j S_j \right), \left(S_1 \sum_{j=1}^{N_f} c_j C_j + d_j S_j \right), \dots, \right. \\ &\quad \left. \left(C_{N_f} \sum_{j=1}^{N_f} a_j C_j + b_j S_j \right), \left(S_{N_f} \sum_{j=1}^{N_f} a_j C_j + b_j S_j \right), \left(C_{N_f} \sum_{j=1}^{N_f} c_j C_j + d_j S_j \right), \left(S_{N_f} \sum_{j=1}^{N_f} c_j C_j + d_j S_j \right) \right]^\top.\end{aligned}$$

From this, we can obtain an explicit matrix representation of $\mathbf{T}_f^\top \mathbf{T}_f$. In particular,

$$\mathbf{T}_f^\top \mathbf{T}_f = \left[\begin{array}{c|c|c|c} \mathbf{Y}_{1,1} & \mathbf{0} & \mathbf{Y}_{1,2} & \mathbf{0} \\ \mathbf{0} & \mathbf{Y}_{1,1} & \mathbf{0} & \mathbf{Y}_{1,2} \\ \hline \mathbf{Y}_{2,1} & \mathbf{0} & \mathbf{Y}_{2,2} & \mathbf{0} \\ \mathbf{0} & \mathbf{Y}_{2,1} & \mathbf{0} & \mathbf{Y}_{2,2} \\ \hline \vdots & \vdots & \vdots & \ddots \\ \hline \mathbf{Y}_{N_f,1} & \mathbf{0} & \mathbf{Y}_{N_f,2} & \mathbf{0} \\ \mathbf{0} & \mathbf{Y}_{N_f,1} & \mathbf{0} & \mathbf{Y}_{N_f,2} \\ \hline \end{array} \right] \dots \left[\begin{array}{c|c} \mathbf{Y}_{1,N_f} & \mathbf{0} \\ \mathbf{0} & \mathbf{Y}_{1,N_f} \\ \hline \mathbf{Y}_{2,N_f} & \mathbf{0} \\ \mathbf{0} & \mathbf{Y}_{2,N_f} \\ \hline \vdots & \vdots \\ \hline \mathbf{Y}_{N_f,N_f} & \mathbf{0} \\ \mathbf{0} & \mathbf{Y}_{N_f,N_f} \\ \hline \end{array} \right], \text{ where } \mathbf{Y}_{i,j}(t) := \begin{bmatrix} C_i(t) C_j(t) & C_i(t) S_j(t) \\ C_j(t) S_i(t) & S_i(t) S_j(t) \end{bmatrix}.$$

This representation reveals that $\mathbf{T}_f^\top \mathbf{T}_f$ is the sum of two rank-1 operators. To see this, define

$$\begin{aligned}\mathbf{v}_1 &:= \frac{1}{\sqrt{N_f}} [C_1 \ S_1 \ 0 \ 0 \ C_2 \ S_2 \ \dots \ C_{N_f} \ S_{N_f} \ 0 \ 0]^\top, \\ \mathbf{v}_2 &:= \frac{1}{\sqrt{N_f}} [0 \ 0 \ C_1 \ S_1 \ 0 \ 0 \ \dots \ 0 \ 0 \ C_{N_f} \ S_{N_f}]^\top.\end{aligned}$$

It is clear that $\{\mathbf{v}_1, \mathbf{v}_2\}$ is an orthonormal system in \mathbb{R}^{4N_f} . Furthermore, it can be shown that

$$\mathbf{T}_f^\top \mathbf{T}_f = N_f (\mathbf{v}_1 \mathbf{v}_1^\top + \mathbf{v}_2 \mathbf{v}_2^\top). \quad (\text{D19})$$

We recognize (D19) as the spectral decomposition of $\mathbf{T}_f^\top \mathbf{T}_f$, implying that $\sqrt{N_f}$ is the only eigenvalue of this matrix. The proof is finished since it follows that

$$\|\mathbf{T}_f\|_2 = \sqrt{N_f}.$$

□

Appendix E A discretized solution operator and its adjoint

Here we derive the action discrete solution operator $\mathbf{S} : \mathbb{R}_M^{n_x} \rightarrow \mathbb{R}_M^{n_x \times n_t}$ from the model (75). Subsequently, we develop an algorithm for computing the action of the adjoint $\mathbf{S}^* : \mathbb{R}_M^{n_x \times n_t} \rightarrow \mathbb{R}_M^{n_x}$.

Consider $\{t_\ell\}_{\ell=0}^{n_t}$, the discretization of T , and define $u_\ell := u(\mathbf{x}, t_\ell)$. Using the implicit Euler scheme,

$$u_t(\mathbf{x}, t_{\ell+1}) \approx \frac{u^{\ell+1} - u^\ell}{\Delta t}, \quad \ell \in \{0, \dots, n_t - 1\}.$$

Substituting this into (75),

$$u^{\ell+1} - \Delta t \alpha \Delta u^{\ell+1} + \Delta t \mathbf{v} \cdot \nabla u^{\ell+1} = u^\ell + a_{\ell+1} \Delta t m, \quad a_{\ell+1} := a(t_{\ell+1}). \quad (\text{E20})$$

Hence, obtaining a solution to (75) amounts to solving an elliptic PDE at each time-step. Now, define the space $\mathcal{U} := \{u \in H^1(\Omega) : u|_{E_0} = 0\}$. Then, the weak form of (E20) is: find $u^{\ell+1} \in \mathcal{U}$ such that

$$\langle u^{\ell+1}, \zeta \rangle + \Delta t \alpha \langle \nabla u^{\ell+1}, \nabla \zeta \rangle + \Delta t \langle \mathbf{v} \cdot u^{\ell+1}, \zeta \rangle = \langle u^\ell, \zeta \rangle + a_{\ell+1} \Delta t \langle m, \zeta \rangle, \quad \text{for all } \zeta \in \mathcal{U}. \quad (\text{E21})$$

We discretize (E21) in space with the finite element method; see Subsection 5.1. Define $\mathbf{A} \in \mathbb{R}^{n_x \times n_x}$ by

$$A_{i,j} := \langle \phi_i, \phi_j \rangle + \alpha \Delta t \langle \nabla \phi_i, \nabla \phi_j \rangle + \Delta t \langle \mathbf{v} \cdot \nabla \phi_i, \phi_j \rangle, \quad i, j \in \{1, 2, \dots, n_x\}.$$

Now, let $\mathbf{u}_\ell \in \mathbb{R}_{\mathbf{M}}^{n_x}$ be the finite element coefficients of the solution at the ℓ -th time and form the snapshot matrix $\mathbf{U} = [\mathbf{u}_1 \dots \mathbf{u}_{n_t}]$. Then, $\mathbf{Sm} = \mathbf{U}$ where \mathbf{u}_ℓ are found by solving

$$\mathbf{A}\mathbf{u}_{\ell+1} = \mathbf{M}\mathbf{u}_\ell + a_{\ell+1} \Delta t \mathbf{M}\mathbf{m}, \quad \ell \in \{0, \dots, n_t - 1\}. \quad (\text{E22})$$

The adjoint. To derive the adjoint, let $\mathbf{a} := [a_1 \dots a_{n_t}]^\top$ and define

$$p_\ell(x; \mathbf{a}) := \sum_{j=1}^{\ell} a_j x^{\ell-j+1}. \quad (\text{E23})$$

We then reveal a recursive relationship and write the result in terms of (E23). Specifically, observe that

$$\begin{aligned} \mathbf{u}_1 &= \mathbf{A}^{-1} \mathbf{M} \mathbf{u}_0 + a_1 \Delta t \mathbf{A}^{-1} \mathbf{M} \mathbf{m} \\ \mathbf{u}_2 &= \mathbf{A}^{-1} \mathbf{M} \mathbf{u}_1 + a_2 \Delta t \mathbf{A}^{-1} \mathbf{M} \mathbf{m} \\ &= (\mathbf{A}^{-1} \mathbf{M})^2 \mathbf{u}_0 + a_1 \Delta t (\mathbf{A}^{-1} \mathbf{M})^2 \mathbf{m} + a_2 \Delta t \mathbf{A}^{-1} \mathbf{M} \mathbf{m} \\ &\vdots \\ \mathbf{u}_\ell &= (\mathbf{A}^{-1} \mathbf{M})^\ell \mathbf{u}_0 + \Delta t p_\ell(\mathbf{A}^{-1} \mathbf{M}; \mathbf{a}) \mathbf{m}. \end{aligned}$$

Assuming that $\mathbf{u}_0 = \mathbf{0}$, the recursive relationship is defined by

$$\mathbf{u}_\ell = \Delta t p_\ell(\mathbf{A}^{-1} \mathbf{M}; \mathbf{a}) \mathbf{m}, \quad \ell \in \{1, \dots, n_t\}. \quad (\text{E24})$$

In the next step we let $\mathbf{V} \in \mathbb{R}_{\mathbf{M}}^{n_x \times n_t}$ and seek \mathbf{S}^* such that $\langle \langle \mathbf{Sm}, \mathbf{V} \rangle \rangle_{\mathbf{M}} = \langle \mathbf{m}, \mathbf{S}^* \mathbf{V} \rangle_{\mathbf{M}}$. Using the identity for $\langle \langle \cdot, \cdot \rangle \rangle_{\mathbf{M}}$ presented in (54a), we have that

$$\langle \langle \mathbf{Sm}, \mathbf{V} \rangle \rangle_{\mathbf{M}} = \mathbf{1}^\top (\mathbf{U} \odot \mathbf{M} \mathbf{V}) \mathbf{w} = \sum_{\ell=1}^n w_\ell \mathbf{1}^\top (\mathbf{u}_\ell \odot \mathbf{M} \mathbf{v}_\ell).$$

Note that for any $\mathbf{m}_1, \mathbf{m}_2 \in \mathbb{R}^{n_x}$,

$$\mathbf{1}^\top (\mathbf{m}_1 \odot \mathbf{m}_2) = \mathbf{m}_1^\top \mathbf{m}_2 = \mathbf{m}_2^\top \mathbf{m}_1.$$

Thus, using (E24), the identity above, then inserting $\mathbf{M}^{-1} \mathbf{M} = \mathbf{I}$ in the right place, we have

$$\begin{aligned} \sum_{\ell=1}^n w_\ell \mathbf{1}^\top (\mathbf{u}_\ell \odot \mathbf{M} \mathbf{v}_\ell) &= \Delta t \sum_{\ell=1}^{n_t} w_\ell \mathbf{1}^\top (p_\ell(\mathbf{A}^{-1} \mathbf{M}; \mathbf{a}) \mathbf{m} \odot \mathbf{M} \mathbf{v}_\ell) \\ &= \left(\Delta t \sum_{\ell=1}^{n_t} w_\ell \mathbf{v}_\ell^\top \mathbf{M} p_\ell(\mathbf{A}^{-1} \mathbf{M}; \mathbf{a}) \mathbf{M}^{-1} \right) \mathbf{M} \mathbf{m} \\ &= \langle \mathbf{m}, \mathbf{S}^* \mathbf{V} \rangle_{\mathbf{M}}, \end{aligned}$$

where

$$\mathbf{S}^* \mathbf{V} := \Delta t \left(\sum_{\ell=1}^{n_t} w_{\ell} \mathbf{v}_{\ell}^{\top} \mathbf{M} p_{\ell}(\mathbf{A}^{-1} \mathbf{M}; \mathbf{a}) \mathbf{M}^{-1} \right)^{\top}. \quad (\text{E25})$$

To obtain a useful representation for the action of $\mathbf{S}^* \mathbf{V}$, we must perform some additional steps. Let $\ell \in \{1, \dots, n_t\}$ and recall the definition of p_{ℓ} given in (E23). Then,

$$\begin{aligned} \mathbf{M}^{-1} p_{\ell}(\mathbf{A}^{-1} \mathbf{M}; \mathbf{a})^{\top} \mathbf{M} &= \mathbf{M}^{-1} \left(\sum_{j=1}^{\ell} a_{\ell} (\mathbf{A}^{-1} \mathbf{M})^{\ell-j+1} \right)^{\top} \mathbf{M} \\ &= \sum_{j=1}^{\ell} a_{\ell} \mathbf{M}^{-1} (\mathbf{M} \mathbf{A}^{-\top})^{\ell-j+1} \mathbf{M} \\ &= \sum_{j=1}^{\ell} a_{\ell} (\mathbf{A}^{-\top} \mathbf{M})^{\ell-j+1}. \end{aligned}$$

Thus, by the definition of (E23), we have that $\mathbf{M}^{-1} p_{\ell}(\mathbf{A}^{-1} \mathbf{M}; \mathbf{a})^{\top} \mathbf{M} = p_{\ell}(\mathbf{A}^{-\top} \mathbf{M}; \mathbf{a})$. Returning to (E25),

$$\begin{aligned} \mathbf{S}^* \mathbf{V} &= \left(\Delta t \sum_{\ell=1}^{n_t} w_{\ell} \mathbf{v}_{\ell}^{\top} \mathbf{M} p_{\ell}(\mathbf{A}^{-1} \mathbf{M}; \mathbf{a}) \mathbf{M}^{-1} \right)^{\top} \\ &= \Delta t \sum_{\ell=1}^{n_t} w_{\ell} (\mathbf{M}^{-1} p_{\ell}(\mathbf{A}^{-1} \mathbf{M}; \mathbf{a})^{\top} \mathbf{M}) \mathbf{v}_{\ell} \\ &= \Delta t \sum_{\ell=1}^{n_t} w_{\ell} p_{\ell}(\mathbf{A}^{-\top} \mathbf{M}; \mathbf{a}) \mathbf{v}_{\ell}. \end{aligned}$$

By examining each term in the resulting sum and expanding $p_{\ell}(\mathbf{A}^{-\top} \mathbf{M}; \mathbf{a})$, we find the recursive relation

$$\begin{aligned} \Delta t^{-1} \mathbf{S}^* \mathbf{V} &= a_1 w_1 (\mathbf{A}^{-\top} \mathbf{M}) \mathbf{v}_1 \\ &\quad + a_1 w_2 (\mathbf{A}^{-\top} \mathbf{M})^2 \mathbf{v}_2 + a_2 w_2 (\mathbf{A}^{-\top} \mathbf{M}) \mathbf{v}_2 \\ &\quad \vdots \\ &\quad + a_1 w_{n_t} (\mathbf{A}^{-\top} \mathbf{M})^{n_t} \mathbf{v}_{n_t} + a_2 w_{n_t} (\mathbf{A}^{-\top} \mathbf{M})^{n_t-1} \mathbf{v}_{n_t} + \dots + a_{n_t} w_{n_t} (\mathbf{A}^{\top} \mathbf{M}) \mathbf{v}_{n_t}. \end{aligned}$$

Factoring the powers of $\mathbf{A}^{-\top} \mathbf{M}$, this becomes

$$\begin{aligned} \Delta t^{-1} \mathbf{S}^* \mathbf{V} &= (\mathbf{A}^{-\top} \mathbf{M}) (a_1 w_1 \mathbf{v}_1 + a_2 w_2 \mathbf{v}_2 + \dots + a_{n_t} w_{n_t} \mathbf{v}_{n_t}) \\ &\quad + (\mathbf{A}^{-\top} \mathbf{M})^2 (a_1 w_2 \mathbf{v}_2 + a_2 w_3 \mathbf{v}_3 + \dots + a_{n_t-1} w_{n_t} \mathbf{v}_{n_t}) \\ &\quad \vdots \\ &\quad + (\mathbf{A}^{-\top} \mathbf{M})^{n_t-1} (a_1 w_{n_t-1} \mathbf{v}_{n_t-1} + a_2 w_{n_t} \mathbf{v}_{n_t}) \\ &\quad + (\mathbf{A}^{-\top} \mathbf{M})^{n_t} (a_1 w_{n_t} \mathbf{v}_{n_t}). \end{aligned}$$

Thus,

$$\mathbf{S}^* \mathbf{v} = \Delta t^{-1} \sum_{\ell=1}^{n_t} (\mathbf{A}^{-\top} \mathbf{M})^{\ell} \sum_{j=1}^{n_t-\ell+1} a_j w_{j+\ell-1} \mathbf{v}_{j+\ell-1}. \quad (\text{E26})$$

From (E26) we derive Algorithm 2; a method for applying \mathbf{S}^* to $\mathbf{V} \in \mathbb{R}_{\mathbf{M}}^{n_x \times n_t}$ with only n_t solves.

Algorithm 2 Algorithm for computing $\mathbf{S}^*\mathbf{V}$

1: **Input:** $\mathbf{V} \in \mathbb{R}_M^{n_x \times n_t}$, $\mathbf{a} \in \mathbb{R}^{n_t}$, $\mathbf{w} \in \mathbb{R}^{n_t}$

2: **Output:** $\mathbf{q} = \mathbf{S}^*\mathbf{V} \in \mathbb{R}_M^{n_x}$

3: Set $\mathbf{q} = \mathbf{0} \in \mathbb{R}^{n_x}$

4: **for** $\ell = 1$ to n_t **do**

5: Compute

$$\mathbf{z} = \mathbf{q} + \sum_{j=1}^{\ell} a_j w_{n_t - \ell + j} \mathbf{v}_{n_t - \ell + j}$$

6: Solve $\mathbf{A}^\top \mathbf{q} = \mathbf{Mz}$ for \mathbf{q}

7: **end for**

8: **return** $\Delta t \mathbf{q}$

The submitted manuscript has been created by UChicago Argonne, LLC, Operator of Argonne National Laboratory (“Argonne”). Argonne, a U.S. Department of Energy Office of Science laboratory, is operated under Contract No. DE-AC02-06CH11357. The U.S. Government retains for itself, and others acting on its behalf, a paid-up nonexclusive, irrevocable worldwide license in said article to reproduce, prepare derivative works, distribute copies to the public, and perform publicly and display publicly, by or on behalf of the Government. The Department of Energy will provide public access to these results of federally sponsored research in accordance with the DOE Public Access Plan. <http://energy.gov/downloads/doe-public-access-plan>.